Experimental and numerical verifications of new methods to predict gasification kinetics of char from MSW (Municipal Solid Waste) components using the TGA

by

Yuvraj Singh Baath

A thesis submitted in partial fulfillment of the requirements for the degree of

Master of Science

in

Chemical Engineering

Department of Chemical and Materials Engineering

University of Alberta

Abstract

Thermogravimetric Analyzer (TGA) is a standard state of the art instrument used for investigating char gasification kinetics. However, one major flaw of the TGA is the build up of a stagnant gas region between the empty space of the crucible mouth and the char sample layer which leads to poor gas-solid contacting. Diffusion is the predominant transport mechanism for transport of the reactive gas from the crucible mouth to the porous char layer. Therefore, the aim of this work is to present a numerical model for evaluating the kinetic data using a TGA, which encapsulates the three diffusion phenomenons of the reactive gas inside the TGA crucible (i) diffusion of gas between the char layer and crucible mouth, (ii) diffusion of gas within the inter-particle voids of the char layer and (iii) diffusion of the gas within the intra-particle pores of the char particle. The model was first formulated and validated for the non-porous char particles and then extended to the porous particles. Experimentally derived kinetic data was used as an initial input for the model and the improved parameters were derived by tuning the model to predict the experimental curves. The consideration of diffusional effects within the crucible resulted in an 8.5% increase in the activation energy.

In the second part of this work, chars are formed using the blends of Softwood and High Density Polyethylene. First, the synergistic effects during the co-pyrolysis of these mixtures are studied using the TGA. It is seen that the synergies between biomass and plastic favour the release of volatiles and reduce the char formation. The synergistic

effects also improve the gasification reactivity of the chars by increasing its carbon content and the BET surface area. Finally, the TGA model is used to determine the kinetic parameters of gasification of these chars. A 3.9% decrease in the activation energy was observed upon increasing the blending ratio of the HDPE from 0 to 50%.

Acknowledgement

First of all, I would like to thank my supervisors, Dr. Rajender Gupta and Dr. Petr Nikrityuk, for providing me this wonderful opportunity of conducting research at UoA, under their supervision. Without their collective faith in me, this would merely have been a dream for me. Thank you Dr. Petr for your everlasting encouragement and invaluable inputs at the every hurdle that I faced during my graduate studies. I would also like to express my sincerest gratitude to Dr. Gupta for providing his invaluable knowledge, suggestions and advice to this research which helped me to shape the experimental progress of this project.

I am extremely grateful for the research group that I was a part of. Thank you Dr. Monir, Dr. Deepak, Ankit, Snehlata, Manjot and Yang Wu for your continuous cooperation while working in the lab and help me learn operate the instruments that I used for conducting my experiments.

I would also like to thank all my friends in Edmonton and back home in India, who have made my time at UoA an unforgettable experience. Life in this pandemic would have been very difficult if I would have not been able to share the time and joy with you guys whether be it in person or virtually.

Last but not the least, I would like to express my gratitude and thank my parents and my sister for their unconditional love, support and belief in me. I owe all my success to the hard work and sacrifices you guys have made, to get me to this point.

Contents

List of Figures

List of Tables

List of Symbols

X = Conversion (-)

t = Time (s)

M = Mass (kg)

R = Reactivity (s^{-1})

k = Kinetic constant ($m\,s^{-1}$)

K_{RPM} = Random pore model reaction rate (s^{-1})

A_0 = Arrhenius constant ($m\,s^{-1}$)

E_A = Activation Energy ($kJ\,mol^{-1}$)

T = Temperature (K)

h = Height of the sample (m)

H = Height of the crucible (m)

D = Diameter of the crucible (m)

N_p = Number of particles (-)

V = Volume of the sample (m^3)

V_p = Volume of the particle (m^3)

R_p = Radius of the Particle (m^3)

S_p = External surface area of a single particle (m^3)

c = Specific capacity ($J\,kg^{-1}\,K^{-1}$)

$\dot{Q}$ = Heat flow rate ($W\,m^{-2}$)

A = Area of sample (m^2)

$\dot{m_C}$ = Carbon Mass flow rate ($kg\,s^{-1}$)

$\Delta_R H$ = Specific reaction enthalpy ($J\,kg^{-1}$)

$\dot{m_C}$" = Carbon mass flux ($kg\,m^{-2}\,s^{-1}$)

Y_i = Species mass fraction (-)

D = Diffusion coefficient ($m^2\,s^{-1}$)

MW_i = Molecular weight ($kg\,mol^{-1}$)

$\dot{m}_{C,V}$ = Volumetric based carbon mass flow rate ($kg\,s^{-1}$)

$\dot{m}_{C,S}$ = Surface based carbon mass flow rate ($kg\,s^{-1}$)

S''' = Volumetric specific surface area (m^{-1})

a_1 = Division constant (-)

R_{pore} = Radius of the pore (m)

W = Weight loss (-)

x = Blending ratio (-)

Greek Letters

ψ = Char structural parameter (-)

ϵ = Void fraction (-)

ρ = Density ($kg\,m^{-3}$)

λ = Thermal conductivity ($W\,m^{-1}\,K^{-1}$)

$\epsilon_{emissivity}$ = sample emissivity (-)

σ_{SB} = Stefan-Boltzmann constant ($W\,m^{-2}\,K^{-4}$)

ϵ_P = Particle porosity (-)

β_{in} = Internal Mass transfer coefficient ($m\,s^{-1}$)

η = Effectiveness Factor (-)

ϕ = Thiele Modulus (-)

Subscripts

0 = initial

∞ = bulk

pm = porous media

pp = porous particle

S = Surface of the char layer

s = solid phase

w = wall of the crucible

P = Particle

g = gas phase

eff = effective

C = Carbon

kn = Knudsen

SW = Softwood

HDPE = High Density Polyethylene

Chapter 1

Introduction

1.1 Background and Motivation

The fossil fuels have fueled our transition to the industrial age for almost three centuries now. Although, it is not known how much fossil fuel is still available, but it generally accepted that it is non-renewable and is being depleted [1]. Other major problem associated with the burning of fossil fuels is global warming, which has life-threatening consequences if the global emissions are not contained immediately. This has forced the governments, all the over the world to push for renewable and carbon neutral sources of energy to meet the ever-growing energy demands of nations [2]. Biomass is one such renewable source or energy that has the potential to cope with the fossil fuel depletion and mitigate the green house gas emissions. Therefore, in the last two decades the thermochemical conversion of biomass has been extensively studied in order to utilize biomass as fuel [3]. Municipal Solid Waste (MSW) which majorly comprises of biomass and plastics as its main components is now viewed not as a waste that needs to be disposed but as a energy recovering source of fuel [4]. Thermochemical conversion of the MSW also provides solution to the problem associated with its disposal.

Gasification as a thermochemical conversion technology is particularly attractive because the syngas produced after treatment can be used for multivarious purposes. If

CO_2 is used as an oxidative medium for the gasification technology, it provides the added benefits of acting as a potential carbon capture and utilization technology (CCU) [5]. Char heterogeneous reaction with the reactive gas is the rate determining step in the gasification process and therefore it is necessary to study the gasification kinetics of char in order to design the gasifier reactors [6]. Therefore, this research work attempts to provide solutions to the limitations associated with the experimental methods used for calculating gasification kinetics of the biochar while also investigating the effects of synergies existing between biomass and plastic components on the char reactivity.

1.2 Research Objectives

Following major objectives were aimed to be accomplished during this study's duration:

- Experimental investigation of the char gasification using CO_2 in a Thermogravemetric Analyzer (TGA)
- Development, Validation and Implementation of a numerical model encapsulating various heat and mass transfer phenomenons within the TGA crucible in order to re-valuate the improved kinetic parameters of char gasification
- Evaluation of synergistic effects between the biomass and the plastic components during their co-pyrolysis.
- Understanding of the effects of these synergies on the reactivity of the char formed using various blends of Softwood and High Density Polyethylene.

1.3 Thesis Outline

The thesis consists of six chapters. The following description outlines each chapter in this thesis:

Chapter 1: Introduces the background, motivation and the overall objectives associated with this study.

Chapter 2: This chapter reviews in detail the available literature on the subject matter. The chapter discusses briefly the thermochemical conversion routes of biomass to energy followed by a comprehensive review into kinetic modeling of char reactivity, state of the art instruments utilized and the problem statement associated with the TGA. At last a brief review is provided on the literature available for co-pyrolysis of biomass and plastic components.

Chapter 3: This chapter lays out a detailed scheme of the experiments conducted in this study. This included feed characterization, char gasification tests in a TGA and co-pyrolysis of SW and HDPE blends using the TGA and the tube funace.

Chapter 4: Chapter 4 in this thesis proposes a novel numerical model of the TGA. The chapter discusses in detail the model formulation, validation, solution methodology and implementation to re-evaluate kinetic experiments from the tests conducted inside the TGA.

Chapter 5: In this chapter, results obtained from the experiments performed using the blends of SW and HDPE are presented and discussed in detail based on the available literature.

Chapter 6: Finally the conclusion provides the outcomes obtained in this study and includes in brief, the possible future work that can be done.

Chapter 2

Literature Review

2.1 Biomass feedstocks: A general overview

Biomass is a contemporaneous and renewable resource unlike fossil fuels, mainly deriving its energy source from a process called photosynthesis. Photosynthesis combines solar energy and carbon dioxide into chemical energy in the form of carbohydrates [1]. Hence, its usage as a fuel is a carbon neutral process since the carbon dioxide captured from the atmosphere during the photosynthesis is used to form the carbon source for energy generation using the thermo-chemical conversion processes. A general classification of biomass can be made based on its source, origin and distinct biological diversity. Table 2.1 classifies biomass into five groups mainly based on source and its biological diversity.

2.1.1 Composition of biomass

Since different biomass groups show vast diversity in terms of their natural origin, structural and elemental composition of biomass varies extensively. Lignocellulosic biomass i.e biomass originating from plant and plant based materials such as woody remains of the forest waste, non-edible parts of crops and other agricultural waste biomass, is abundantly available in the nature and is at the forefront of research activities based

on energy generation through biomass worldwide [7].

Table 2.1: Biomass classification based on existence in nature [8]

Biomass groups	Subgroups and species
Woody biomass	forest tree residue:barks, branches, leaves, stems; mill residue:lumps, off-cuts, sawdust, sawmill; wood pellets, chips and other wood species
Herbaceous and agricultural biomass	grasses: weed, cane, bamboo etc.; straw crops: corn, soya bean, wheat, rice, millet, flax, barley etc.; other residue: shells, husks, kernels, pulps, bagasse etc.
Aquatic biomass	marine algae: macroalgae(blue, green, brown, red), microalgae; others: seaweed, kelp, water hyacinth, marine dead remains, coral reefs etc.
Industrial biomass waste(semi-biomass)	municipal solid waste, refuse-derived fuel, sewage sludge, paper-pulp sludge, waste papers
Other biomass	animal waste, various manures, bones, meat etc.

Structural composition of lignocellulose biomass

Polymers having extensive chains of carbon atoms linked to macromolecules form basic structural composition of biomass [1]. Chemical bonds linking carbon with carbon, or carbon with oxygen, or sometimes other elements such as nitrogen and sulfur form the backbone of the polymer. The three main components of lignocellulosic biomass are cellulose (40-60%), hemi-cellulose (20-40%), and lignin (15-35%). Besides these, a small

fraction of inorganic mixture is also present [9].

Cellulose is a long chain linear polysaccharide with the molecular formula $(C_6\,H_{10}\,O_5)_n$, a high molecular weight and forms the main part of the cell wall of the plant's cell. It is composed of two β-glucopyranose units and the framework is linked by β-1,4-glycosidic bonds [10]. Hemicelluloses are heteropolysaccharides and act as a linkage between cellulose and lignin ([7],[9]). Their composition varies depending upon the type of biomass and their molecular weight is lower than that of cellulose [11]. Lignins are a complex and amorphous aromatic polymer with a three-dimensional network composed of different phenylpropane units. The units are connected by different ether and carbon to carbon linkages. It is concentrated between outer layers of the fibres, leading to structural rigidity of the plant structure ([1], [12]).

Elemental composition of biomass

Any biomass consists of carbon(C), hydrogen(H), oxygen(O), nitrogen(N) and sulphur(S) as its main elemental constituents. A small amount of inorganic components such as calcium, sodium, potassium, magnesium, phosphorus, silicon etc. are also present which contributes to the ash formation during its thermo-chemical conversion [13]. As photosynthesis converts CO_2 into carbohydrates, carbon is obviously the most important constituent of lignocellulosic biomass and the decreasing order of abundance of these elements in biomass commonly follows C (40-60%), O (30-50%), H (1-10%), N ($< 1\%$) and S ($< 1\%$) ([8], [9], [13]). Proximate analysis of typical biomass samples suggest that it has a higher content of volatiles as compared to coal but a lower fixed carbon content [14].

2.1.2 Energy from biomass

As discussed earlier, biomass stores solar energy in the chemical form and through conversion processes, this energy can be converted into different type of energy carriers. Fig.2.1 classifies three major conversion routes that can be employed to produce energy and utility chemicals from biomass. Type of biomass feedstock available, the type of fuel required and the cost the process are the few important parameters which contribute majorly in deciding the conversion technology to be implemented for production process [7].

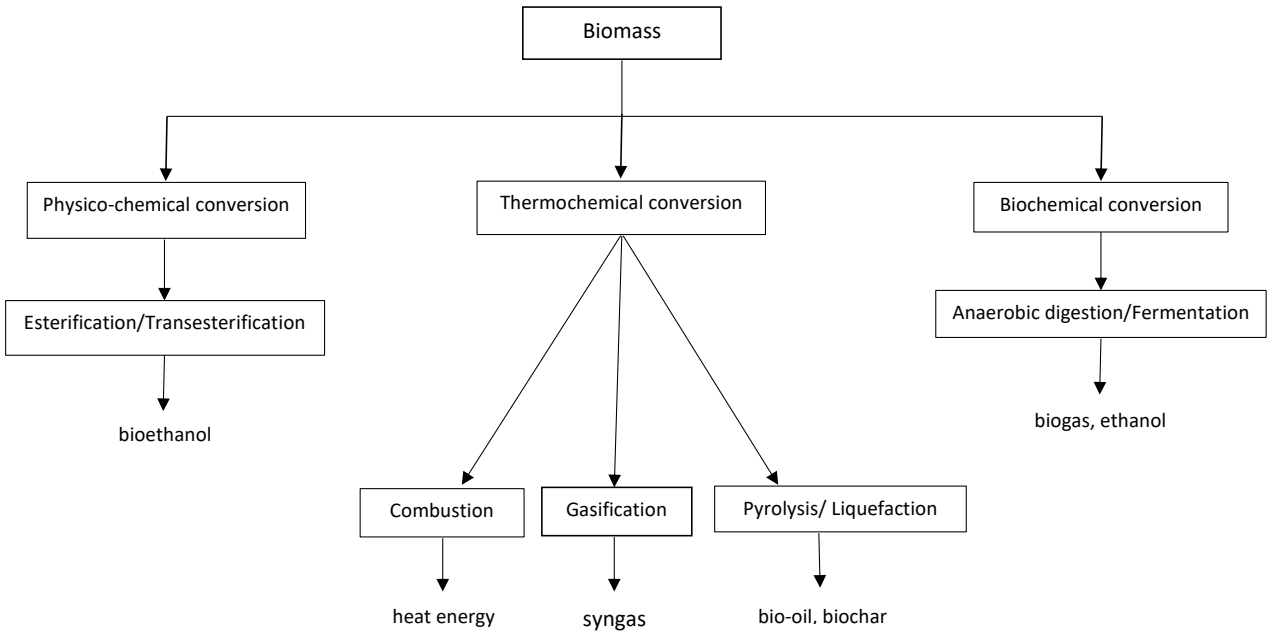

Figure 2.1: Different conversion routes for biomass to energy [7], [15]

Physico-chemical route

Physico-chemical route of biomass conversion uses first generation biomass such as vegetable oils, cooking oils and animal fats and converts them into biodiesel through esterification and/or transesterification process. In this process, the triglycerides of oil

are converted into methyl or ethyl esters using methyl or ethyl alcohol in the presence of an alkaline catalyst [16]. The production of first generation biofuels is a well established process, however the biomass sources for this process come in direct competition with the food industry in terms of land and water usage for their cultivation. This may cause economical imbalance in the food industry and society in general [17].

Biochemical route

Biochemical route involves the enzymatic transformation of cellulose and hemi-cellulose to sugars and subsequent fermentation to bioethanol [18]. Another popular biochemical technology is anaerobic digestion in which mixed culture enzymes are used to break down biomass to produce biogas [9]. This process is popularly used in the municipal waste management. This route is less prone to commercialization yet and much needs to be done in reducing costs, improving efficacy of enzymes and improving overall process integration. Although, with recent research trends in new sources of enzymes and their cocktail preparation, this technology has made major advancements in terms of capital cutting by making enzyme production cost effective [19].

Thermochemical routes

The thermochemical conversion involves applying heat and chemical processes to obtain energy from biomass. Generally, thermochemical conversion technologies are classified into combustion, pyrolysis, liquefaction and gasification [17].

Combustion

Like coal, biomass can be directly combusted in power plants to produce heat energy. Combustion is the sequence of exothermic chemical reactions between the fuel and excess air accompanied by the production of heat and conversion of chemical species. Although biomass combustion is a complex process, the main process steps are drying, devolatilization, char combustion and gas phase oxidation [20]. It is the best established

and most commonly used technology for converting biomass to heat. The combustion efficiency depends primarily on good contact between the oxygen in air and the biomass fuel.

Pyrolysis

Pyrolysis is the process of degradation of biomass by heat in the absence of oxygen resulting in the production of liquid(bio-oil), gaseous(combustible gas) and solid(char) products [21]. In all the thermo-chemical conversion routes, kinetics of biomass pyrolysis play a key role in reactor design and determining product distribution [15]. Independent pyrolysis of components of biomass by Wei et al. [12] gave temperature ranges for thermal decomposition of cellulose, hemicellulose and lignin. Hemicellulose degradation starts first around $170\,^0C$ followed by cellulose around $270\,^0C$. For both hemicellulose and cellulose, almost all degradation takes place in a narrow temperature range uptill $400\,^0C$ whereas lignin degradation takes place over a broader range and continues beyond $700\,^0C$. Based on the residence time of the particles in the reactor, heating rate and final temperature, pyrolysis process can be further classified into slow pyrolysis, intermediate pyrolysis and fast pyrolysis [1].

Slow pyrolysis is characterized by low heating rates and residence time of hours with maximum temperature around $400 - 600\,^0C$. It yields char as its major product. Fast pyrolysis, predominantly used for production of bio-oil, is performed at elevated temperatures ($550 - 900\,^0C$), high heating rates and short residence time of vapors less than 1 s ([1],[15]).

Liquefaction

Liquefaction, also known as Hydrothermal Liquefaction (HTL), like pyrolysis is carried out in an oxygen deficit environment but at relatively lower temperatures and high operating pressures. It is the thermochemical conversion of biomass in a hot, pressurized water environment. Sufficient residence time allows for breakdown of solid polymeric structure to liquid components [22]. Optimum temperature condition for different feed-

stocks lies in the range $275 - 375\,^0C$ and pressure usually varies from 4-25 MPa [23].

Gasification

Gasification is the high temperature($> 700\,^0C$) conversion of biomass into gaseous products called synthesis gas or syngas comprising mostly of CO and H_2 depending upon the gasification agent [24]. It is different from combustion due to the fact that if oxygen or air is employed as the agent in a gasifier, only partial amount of stoichiometric requirement (30-40%) is fed into the reactor. While the main purpose of combustion process is the production of heat energy, gasification is primarily used for syngas production which can then be either directly combusted or used as a basis for value-added products such as methanol, synthetic natural gas, dimethyl ether etc [7]. LCA of different thermochemical technologies either for fuel production or as waste management technologies, suggest that the gasification technology has considerable environmental benefits in terms of emission when compared with the combustion process ([25],[26]).

2.2 Fundamentals of Gasification

2.2.1 Gasification steps and reactions

Irrespective of the gasifying agent, three basic steps can characterize the gasification process [24]. These are:

- Drying: In this step all the inherent moisture in biomass is released as the temperature increases past $100\,^0C$. Since it an endothermic step, usually feedstock with high moisture content are not processed using gasification [27].

- Pyrolysis: As discussed in the previous section, as the temperature increases past $250\,^0C$, thermal degradation of biomass starts, which is accompanied by release of volatile products in form of tars and gases, leaving behind a solid product known as char.

- Char gasification and reduction: This is the rate determining step of the gasification process and determines the final conversion achieved in the process. In this step, solid char particles react heterogeneously with gasification medium forming gaseous products. As the temperature increases past $700\,^0C$, kinetics of heterogeneous reaction become dominant and control the gasification rate. Different sets of reaction may take place depending upon the medium of gasification agent [28]. Usually, the selection of gasification medium is governed by the composition of syngas desired.

Different gasification mediums include air, pure oxygen, steam, carbon dioxide or a mixture of these agents. Major gasification reactions with their respective reaction enthalpy which influence the composition of syngas are presented in Table 2.2. As can be seen from gasification reactions, major constituents of syngas are CO and H_2.

Table 2.2: Major gasification reactions (+ve reaction enthalphy means an exothermic reaction and -ve reaction enthalpy means an endothermic reaction). [28],[29]

Heterogeneous gasification reactions	
Carbon oxidation	$C_s + O_2 = CO_2 + 406\,kJ\,mol^{-1}$
Carbon partial oxidation	$C_s + \frac{1}{2}O_2 = CO + 134\,kJ\,mol^{-1}$
Boudouard reaction	$C_s + CO_2 = 2CO - 172\,kJ\,mol^{-1}$
Water gas reaction	$C_s + H_2O = CO + H_2 - 131\,kJ\,mol^{-1}$
Methane formation reaction	$C_s + 2H_2 = CH_4 + 75\,kJ\,mol^{-1}$
Homogeneous gasification reactions	
Carbon monoxide oxidation	$CO + \frac{1}{2}O_2 = CO_2 + 284\,kJ\,mol^{-1}$
Water gas shift reaction	$CO + H_2O = CO_2 + H_2 + 42\,kJ\,mol^{-1}$
Methane oxidation	$CH_4 + 2O_2 = CO_2 + 2H_2O + 808\,kJ\,mol^{-1}$
Methane steam reforming	$CH_4 + H_2O = CO + 3H_2 - 206\,kJ\,mol^{-1}$
Methane dry reforming	$CH_4 + CO_2 = 2CO + 2H_2 - 247\,kJ\,mol^{-1}$
Hydrocarbon steam reforming	$C_nH_m + mH_2O = mCO + (m + n/2)H_2$

Gasification of biomass in air, produces syngas diluted with nitrogen having a heating value of 4-7 MJ/m^3. Using pure O_2 as an oxidant is an expensive alternative due to the costs associated with separating O_2 from air. Therefore, steam and CO_2 have emerged as interesting mediums for producing enhanced quality syngas with heating value of 10-18 MJ/m^3 [29]. Steam promotes the water gas and water gas shift reactions, thus the syngas produced is rich in quality with H_2. On the other hand CO_2 promotes boudouard reaction, producing syngas with CO as its major component. Utilization of CO_2 as a gasifying agent is gaining an expedited interest among scientists because of its potential to be used as a carbon capture and utilization(CCU) technology. CO_2 as a gasfication agent also has additional advantages, including, improved char properties making char reduction more efficient, enhanced syngas properties and reduced tar formation [30].

2.2.2 Classification of gasification reactors (gasifiers)

Gasifiers are mainly classified based on the basis of their gas-solid contacting mode. Based on this, gasifiers are broadly divided into three principal types: (i) fixed bed, (ii) fluidized bed, and (iii) entrained-flow bed [24]. Usually, the fixed bed gasifiers are easy to operate and handle and therefore, are used for small scale applications. For medium to large scale operations, either fluidized or entrained flow gasifiers are preferred as they offer an intensive contact between the gas and biomass particles [31]. A detailed description of the commercial subdivisons of these gasifiers is provided in Table 2.3.

Table 2.3: Description of different type of gasifiers ([15],[24],[28],[31],[32],[33])

Gasifier type	Properties, Advantages and Limitations
Fixed bed gasifiers	
(i) Updraft gasifiers	Fuel is fed in at the top and moves downward while the gasification agent moves counter-currently from the bottom to the top of the reactor. Gases are collected at the top. The main advantage of the reactor is its simplicity in design and low investment costs. Limitations include high tar content in syngas making it unsuitable for engine applications.
(ii) Downdraft gasifiers	These reactors are characterized by the co-current downward movement of both the fuel and gasification agent. The syngas is collected at the bottom of the reactor. This helps to lower the tar content in the product gas. However the product gas exits at relatively high temperature, thereby decreasing the thermal efficiency of the syngas if an external heat recovery system is not employed.
(iii)Crossdraft gasifiers	In Crossdraft gasifiers, gasification medium is injected through a nozzle from the side of a reactor and gas is collected from the opposite side of the entry point. This type of design allows for high gasification temperatures ($> 1500\ ^0C$) to be achieved within the reactor. Advantages include low tar content in the syngas produced, shorter start up times and easy to handle load changes. But these are less suitable for high-ash and high-tar fuels and are mostly used for dry biomass fuels.
Fluidized bed gasifiers	
(i) Bubbling Fluidized bed	In a bubbling fluidized bed gasifier, gasifying agent is injected at the bottom of the grate at a sufficient velocity to keep the bed in state of suspension. The fluid mechanic behaviour is characterized by gas bubbles which are responsible for excellent mixing behaviour within the gasifier. A uniform temperature between $700 - 900\,^0C$ is maintained within the reactor. Advatntages include low tar content syngas and high carbon conversion efficiency. However operation at temepratures $> 900\ ^0C$ may cause bed agglomeration due to low ash melting behaviour.
(ii) Circulating fluidized bed	In CFBs, superficial velocity is significantly more than the terminal velocity. As a result suspension is no more possible and bed particle are spread throughout the reactor. The entrained particles may be carried out of the bed. They are then collected by a cyclone and then returned to the bed. An additional advantage of CFB to the bubbling type is that it may be used for large scale gasification projects.
Entrained flow gasifiers	These are high pressure gasifiers, where reactions occur in a dense cloud of very fine particles. The fuel and medium move co-currently downwards, with temperature within the reactor ranging between $1200 - 1500\,^0C$. The major disadvantages of EFG are the pretreatment costs required to formulate fine particles from biomass feedstock and the short residence time of the particles.

2.3 Char reactivity and its kinetic modeling

As discussed in section 1.2.1, heterogeneous conversion of char into gaseous products is the slowest step in the gasification process. Hence, the insight of the mechanisms of this step become critical while evaluating the overall gasification process and in the designing of the gasifiers. Heterogeneous reactions follow a general mechanism of chemical transformation occuring in several steps [34]. For gasification of char particles these steps can be explained as:

1. External transfer of gasification agent from the bulk to the external surface of the particle
2. Diffusion of gasification agent through the char layer and within the pores of the particle
3. Chemisorption of agent on an active site
4. The intrinsic chemical reaction
5. Product desorption from an active site
6. Diffusion of products through the char layer to the external surface
7. The external transfer back of the products from the external surface to the bulk

Based on these steps, three main regimes can be used to classify the char gasification [35]. Regime I occurs at low temperatures and small particle sizes, so that the external transfer and diffusion steps are much faster than the intrinsic chemical reaction rate. In this case, gasification is said to be kinetically controlled. Regime II occurs when the temperature and the particle size increase and the reactive gas isnt able to completely penetrate the particle. Both diffusion and kinetics of the reaction contribute to the gasification rate. Regime III occurs at very high temperatures, during which the intrinsic reactivity of the char is very high and the external mass transfer is the limiting step.

The instantaneous reaction rate R of the char gasification can be defined mathematically as [36]:

$$R = -\frac{1}{M}\frac{dM}{dt} = \frac{dX}{dt} \tag{2.1}$$

where M is the mass of the the char sample and X is the degree of conversion. It is a well established fact that char reactivity increases with an increase in temperature [37]. Other variables which majorly affect reactivity are the partial pressure of gasifying agent and the char surface area [6]. Therefore the expression for reactivity should encapsulate its dependence on temperature, partial pressure of the gasification agent and the evolution of char surface area with conversion. A general expression for the reaction rate, taking these variables into account appears as follows [38]:

$$\frac{dX}{dt} = k(T)\, G(P_{agent})\, f(X) \tag{2.2}$$

where k(T) is temperature dependent rate constant, G(P_{agent}) is the gasification agent partial pressure function which represents it effect on reactivity and f(X) is the structural term implictly or explicity desrcibing the effects of available internal surface.

There are two approaches to model kinetic rate constant and pressure dependent function [39]. If the gasification agent is only steam or CO_2 and the char sample size is not large such that the products formed from gasification do not have inhibiting effect over the reactivity, then a simple global reaction rate suffices the reactivity expression. In this case, k(T) can be described by an Arrhenius law and a power law may be used to describe the partial pressure function.

$$k(T) = A_0 \exp\frac{-E_A}{RT} \text{.....} (Arrhenius\ law) \tag{2.3}$$

$$G(P_{CO_2\, or\, H_2O}) = P^n_{CO_2\, or\, H_2O} \text{.....} (Power\ law) \tag{2.4}$$

For the case, where a mixture of gases is used as a gasification agent or the product concentration is large enough to cause an inhibiting effect on the rate, Langmuir-Hinshelwood mechanism is used to model the kinetic constant. An example of the L-H

mechanism of CO_2 gasification of the char taking into account CO's inhibiting effect is provided below [40].

$$C_f + CO_2 \xrightarrow{k_1} C(O) + CO$$
$$C(O) + CO \xrightarrow{k_2} C_f + CO_2$$
$$C(O) \xrightarrow{k_3} CO$$

where k_1, k_2 and k_3 are the usual arrhenius rate constants. C_f corresponds to an active carbon site over which adsorption occurs, C(O) is a carbon-oxygen complex. The inhibiting effect of CO is then accounted in the kinetic expression as follows:

$$k(T)\, G(P_{CO_2}) = \frac{k_1\, P_{CO_2}}{1 + (k_2/k_3)\, P_{CO} + (k_1/k_3)\, P_{CO_2}} \tag{2.5}$$

Kinetic parameters using Eq. 2.2 are obtained using a known model f(X) and performing isothermal gasification experiments at different temperatures and partial pressures of the gasification agent and then fitting the chosen model to the retrieved experimental data to obtain the parameters. Different models have been proposed for this approach. These models have been discussed in detail in the following subsection.

2.3.1 Kinetic Models

Models encapsulating the char surface area effect on the reactivity, are of two types: i) Volumetric and ii) Structural [6]. Structural type models explicitly take into account the modifications taking place in the internal pore structure during conversion whereas volumetric type models empirically correlate these changes with conversion and do not account them explicitly into their expressions. Different kinetic models that are used by researchers to define kinetics are discussed below.

Volumetric Model

The volumetric model (VM) is the simplest model describing heterogeneous reactions. It assumes that the chemical reaction takes place simultaneously at all active sites which

are uniformly distributed within the particle. For VM, the reaction rate decreases lineraly with conversion and the overall expression is given by [41]:

$$\frac{dX}{dt} = K_{VM}\,(1 - X) \tag{2.6}$$

Due to its simplicity, it is widely used to model experimental results [42]. However, when compared with other models, its fit for the experimental data is more deviating especially for conversions > 0.7.

Shrinking Core Model or Grain Model

The Shrinking core model (SCM) also known as the Grain model developed by Szekely and Evans [43] assumes that the porous particle consists of an assembly of uniform nonporous grains and the reaction initially occurs on the external surface of the particle and gradually moves in towards the core. The reaction rate expression for this case is given by:

$$\frac{dX}{dt} = K_{SCM}\,(1 - X)^m \tag{2.7}$$

where m depends on the shape of the assumed grain particles. For spheres, m=2/3 and for cylinders, m=1/2. When gasification is performed at high temperatures, and external mass transfer is the limiting step (Regime III), SCM suitably describes the morphology change of the char particle [44].

Integrated Core Model

The integrated core model (ICM) also known as the power law model, is the generalization of the SCM and the VM models and adds an additional parameter relating to reaction rate as n. The char reactivity expression is hence given by [36]:

$$\frac{dX}{dt} = K_{ICM}\,(1 - X)^n \tag{2.8}$$

Random Pore Model

Many researchers have reported a maximum value of reactivity as conversion of char proceeds ([39], [45]). There are three preliminary reasons cited in the literature for this

[39].

- Most researchers perform isothermal tests to obtain kinetics wherein they reach a specific temperature using an inert gas and then switch to reactive agent for char consumption. This leads to non uniform concentration of agent at the beginning of the gasification, which may be responsible for maximum gasification rate.

- Another reason which has been cited in literature is based on gas sampling and analyzing. For experiments where produced gas is used to measure conversion and reactivity, gas mixing in sampling lines is attributed to maximum reaction rate.

- Finally, the maximum gasification reaction rate is attributed to the change in the char reactive surface area during the gasification.

The previous models discussed i.e VM, SCM and ICM do not describe this phenomenon of maximum value of reaction rate. Due to this, many kinetic studies use Random pore model (RPM) developed by Bhatia and Perlmutter [46].
The RPM model considers the competing effects of pore growth during the initial stages of reaction and the destruction of pores due to the coalescence of adjacent pores. Therefore this model predicts the maximum gasification rate as the reaction proceeds. The rate expression for this model is given by:

$$\frac{dX}{dt} = K_{RPM}\,(1-X)\,\sqrt{1-\psi\,ln(1-X)} \tag{2.9}$$

where ψ represents a fitting parameter that describes the internal structure of the non-converted char particle. It is dependent on the surface area (S_0), pore length (L_0) and particle's porosity (ε_0) and can be calculated using:

$$\psi = \frac{4\,\pi\,L_0\,(1-\varepsilon_0)}{S_0^2} \tag{2.10}$$

The ψ value of a char is highly influenced by the pyrolysis method of the char and may even vary for chars formed from the same biomass source. If the value of ψ is close

to zero, it means that the initial char sample is highly porous and therefore, there will be negligible pore growth during the gasification. A high ψ value means that the pore growth is strong with the progress of the reaction [47]. Using experimental results, the value of ψ can be calculated using the following equation [48]:

$$\psi = \frac{2}{2\,ln(1 - X_{max}) + 1} \tag{2.11}$$

where X_{max} is the conversion where the maximum reactivity is observed during experiments. Some authors ([47],[49]) have also used an alternative approach of regression analysis to determine ψ using the least square method by defining a reduced time, $t/t_{0.5}$ i.e the ratio of time (t) to the time required for conversion to reach 0.5 ($t_{0.5}$). Using eq. 2.9, the reduced time can be defined as:

$$\frac{t}{t_{0.5}} = \frac{\sqrt{1 - \psi\, ln(1 - X)} - 1}{\sqrt{1 - \psi\, ln(1 - X_{0.5})} - 1} \tag{2.12}$$

The structure factor was then obtained by fitting eq. 2.12 to the corresponding experimental results using the regression analysis. Due to its ability to predict maximum gasification rate at the beginning, it has been widely utilised to model char gasification and often provides the best fit when compared with the previously discussed methods ([45], [50], [51]). (citations needed)

Modified Random Pore Model

Despite numerous studies satisfactorily using the RPM model to fit the experimental data, there have been some limitations reported in the literature, regarding its effectiveness, especially when the peak reaction rate is observed at high conversion values ([38], [52]). To overcome this inefficiency of the RPM, sevral modifications and extensions to the original RPM have been made by authors.

Zhang et al. [53] modified the RPM by adding an another parameter n, dependant on the structure and the porosity of the solid reactant and successfully implemented it to fit the char gasification experiments. The reactivity expression in this case is given by:

$$\frac{dX}{dt} = K_{RPM}\,(1 - X)^n \sqrt{1 - \psi\, ln(1 - X)} \tag{2.13}$$

Wang et al. [41] also implemented this modified version of RPM to fit their gasification rates and concluded that M-RPM was the best fit model for describing the gasification rate.

Another modification to RPM was made by Zhang et al. [54] to take into account the catalytic effect of alkali metals present within the char. The modification was made by inroducing a new conversion term with two dimensionless parameters into the original the random pore model as indicated below:

$$\frac{dX}{dt} = K_{RPM}\,(1-X)\,\sqrt{1-\psi\,ln(1-X)}(1\,+\,(CX)^p) \tag{2.14}$$

Cortazar et al. [52] determined kinetic parameters for gasification of pine sawdust char using different kinetic models and concluded that M-RPM provided the best fit among all the models. A summary of the above discussed models is provided in Table 2.4

2.4 State of the art in measurement of the heterogeneous kinetics of char gasification

Different state of the art instruments have been employed by researchers to study kinetics of char gasification. Major types include Fixed bed reactors, Fluidized bed reactors, Drop tube furnace (DTF) and Thermogravimetric Analyzers (TGA). A review of the studies published on char gasification kinetics using these instruments is conducted below.

2.4.1 Fixed bed reactor studies

Fixed bed reactors are widely employed in small scale gasifcation units. Studying char gasification in these reactors allow for variations in mass of the sample used and size of the biochar particles that can be gasified. These can be used to model industrial gasification conditions. Ahmed et al. [45] studied woodchips char gasification with steam and CO_2 in a fixed bed reactor. A comparative study of the gasification agents and

Table 2.4: Summary of common isothermal kinetic models

Kinetic Model	Reactivity Expression
Volumetric Model	$\frac{dX}{dt} = K_{VM}(1-X)$
Shrinking Core Model	$\frac{dX}{dt} = K_{SCM}(1-X)^{2/3}$
Integrated Core Model	$\frac{dX}{dt} = K_{ICM}(1-X)^{n}$
Random Pore Model	$\frac{dX}{dt} = K_{RPM}(1-X)\sqrt{1-\psi\, ln(1-X)}$
Modified Random Pore Model	
(i)	$\frac{dX}{dt} = K_{RPM}(1-X)^{n}\sqrt{1-\psi\, ln(1-X)}$
(ii)	$\frac{dX}{dt} = K_{RPM}(1-X)\sqrt{1-\psi\, ln(1-X)}(1+(CX)^{p})$

effect of their partial pressure on the gasification rate was conducted. It was found that for the same sample mass, average gasification rate for steam gasification was almost twice that of CO_2. Also varying partial pressure of both steam and CO_2 had no effect on gasification rates. Random pore model (RPM) was used to fit the reaction rates and obtain average rate constant. Woodruff et al. [55] developed a novel kinetics measurement technique based on a modified fixed bed reactor. This technique allowed for collection of data at high gasification temperatures while limiting heat and mass transfer effects. L-H model was then used to estimate kinetic parameters. Sircar et al. [50] performed CO_2 gasification of pinewood char in a fixed bed using large particles with relevance to practical gasifiers and investigated the char structure development. Data was fitted using different kinetic models to obtain kinetic parameters. RPM provided the best fit with the experimental data. BET study of the chars at different conversion points agreed with the RPM prediction of increasing char surface area initially as the reaction proceeds. After a maximum surface area is recorded, the surface area decreases as the conversion increases. Similarly, Hernandez et al. [42] studied CO_2 gasification kinetics of spent tyre char in a fixed bed apparatus and calculated kinetic parameters by fitting different kinetic models. Zhou et al. [56] investigated CO_2 gasification of brown coals and biomass chars and calculated reaction orders for different feeds. All the reaction orders were less than 1, in the range of 0.3-0.7.

2.4.2 Fluidized bed reactor studies

Fluidized bed reactors (FBR) are also extensively used for gasification studies because of their direct relevance to industry. Nilsson et al. [57] investigated gasification reactivity of char from dried sewage sludge (DSS) performing in-situ gasification experiments in a fluidized bed reactor at different temperatures and partial pressures of CO_2 and steam. Kinetic parameters were obtained using an empirical expression formulated by the author. Upon comparison with reactivity of an ex-situ char generated by the same pyrolysis method, it was found that in-situ gasification of chars showed higher

reactivity than the ex-situ chars. The same group also studied gasification of char from olive tree pruning in a FBR [58] using mixtures of H_2O, CO_2, H_2, CO and N_2 in various proportions to gauge the inhibiting effects of H_2 and CO. L-H model was used to model kinetics dependence on temperature and concentration of gasifying agent and the ICM model was used to account the char morphology change with conversion. Guo et al. [51] used a micro fluidized bed (MFB) to perform in-situ gasification tests on different coal chars. SCM and RPM models were used to fit the experimental data and obtain kinetic parameters. On comparison with ex-situ chars, in-situ chars showed higher reactivity therefore suggesting that cooling and reheating may change chemical structure of the char which causes deactivation. Wang et al. [59] also used a similar MFB methodology to study coal char gasification and fitted the experimental data with VM and SCM models. Tong et al. [60] also used a fluidized bed reactor to study lignite char gasification in CO_2, H_2O and their mixtures. They found that CO_2 and H_2O compete for the same active reaction sites on the char surface. SCM and VM were used to calculate kinetic parameters with the SCM providing a better fit than the VM model.

2.4.3 Drop tube furnace reactor studies

In Drop tube furnaces (DTF), particles fall through a tube and come in contact with the reaction gas either co-currently or counter-currently. The contacting is similar to fludized bed or entrained flow gasifiers, therefore it has developed increasing interest among scientist to study gas-solid reactions. DTFs are characaterized by high heating rates, high operation temperatures and short residence times of the praticles [61]. Hence, pore diffusion may play an important role in the char reactivity and the kinetics determined using DTFs are usually apparent reaction kinetics instead of intrinsic reaction kinetics. Ahn et al. [62] confirmed this fact by studying gasification kinetics of an Indonesian sub-bitumnous coal-char with CO_2 in a pressurized drop tube furnace reactor. The author investigated reactivity of char at different temperatures and

partial pressures of the CO_2 and determined kinetic parameters using the SCM model. Two different activation energies were determined for the range of $900 - 1100\,^0C$ and $1100 - 1400\,^0C$ as the reaction was deemed to be kinetically controlled and pore diffusion limited for the two temperature ranges. Kajitani et al. [63] also reported similar findings for two different coal chars. Matsumoto et al. [64] used DTF to study gasification of different biochars in steam and CO_2 atmospheres. It was observed that the diameter of the char particles nearly remained the same for X$\leq$0.8 regardless of the gasifying agent. RPM was used to fit the experimental data and obtain the kinetic parameters. Upon investigating rice husk char gasification with steam in a DTF, Zhai et al. [65] found that for temperatures less than $850\,^0C$, kinetics could be defined using SCM and VM but for temperatures above $850\,^0C$, this was not the case and concluded that pore diffusion controlled the overall reaction for temperatures above $850\,^0C$. Gonzalez et al. [66] used a novel pressurized drop tube test facility to investigate gasification behaviour of lignite char under CO_2 at different temperatures and partial pressures of CO_2. Samples of char at different reaction times were subjected to different analysis to determine the evolution of the char surface area and pore development with conversion. Kinetic expression for char gasification was obtained by fitting experimental data using the RPM.

2.4.4 Thermogravimetric analyzer studies

The kinetic studies based on the above described reactors have one common theme among them, that the reactivity is measured mostly using gas sampling and analysis. Calculating conversion using gas analysis is difficult and requires extreme precision. As discussed earlier, mixing of gas in the sampling lines may lead to a maximum gasification rate by and leads to error in calculation of conversion as this phenomenon lowers the amount of detected gas [39]. Thermogravimetric analyzers (TGA) avert this step of gas sampling by directly measuring the change of mass of the sample with time. In a TGA, the sample is placed in a sample holder, also known as the crucible which is then

subjected to the reactive environment. The weight of the sample is then continuously monitored as the reaction proceeds. This allows the direct measurement of conversion of the char according to the following equation:

$$X = \frac{M_0 - M_t}{M_0 - M_{ash}} \tag{2.15}$$

here M_0 is the initial mass of the sample, M_t is the mass of the sample at time t and M_{ash} is the mass of the ash content of the sample. Due to it being logistically easier to operate and interpret the data, TGA is the most extensively used instrument for studying char gasification kinetics. Senneca et al. [67] used TGA to study biomass pyrolysis, char combustion and char gasification of three different biomass. The reactivity of olive husk was highest amongst the three biomass fuels investigated. The high reactivity of the olive husk was related to its high mineral content of the ash which acts as a catalyst. The activation energy and reaction order were then determined using the power law relation. Huang et al. [40] used L-H mechanism to define kinetics of char gasification in CO_2-CO and H_2O-H_2 mixtures using a TGA. Malekshahian et al. [49] used a high pressure TGA unit to study petcoke char gasification in CO_2 atmosphere and modeled the kinetics using the RPM model. The reaction order with respect to CO_2 partial pressure was determined to be 0.49 while the total pressure of the gas had insignificant effect on the reactivity. Lin et al. [47] used TGA to study reactivity of chars prepared using different pyrolysis mechanisms for temperatures below $1000\,^0C$ and then proposed an improved aerosol-based method for prediction of reactivity at higher temperatures. The author showed good applicability of the aerosol-gel-method to extrapolate reactivity between the temperature range of $1000\,^0C - 1300\,^0C$. The RPM model was used to determine kinetics of different chars produced. The activation energies for chars from similar biomass were reported to be in a similar range. Gonzalez et al. [68] studied the effect of ash composition on the reactivity of chars from three type of biomass. The catalytic effect of the ash was significant when the conversion of char was greater then 0.8. None of the three models i.e VM, SCM and RPM were able to predict similar reactivity to the one determined experimentally for high conversions. Hence, a modification to the

SCM model was suggested by the author which takes into account this catalytic effect of the ash composition. A similar study on biochars from different garden waste leaves performed by Gupta et al. [69] also showed that biochars with high alkali content showed higher reactivity as compared with chars of low alkali index. The author also studied the effects of addition of external catalyst (K_2CO_3) upon the gasification rate of biochars. The catalyst significantly increased the gasification rate for all biochars upto 20 % loading. Xu et al. [70] investigated CO_2 gasification properties and kinetics of four types of biomass chars using non-isothermal TGA experiments. The author also reported that ash composition had significant catalytic effects on gasification reactivity. Among different kinetic models implemented to obtain kinetic parameters, RPM gave the best fit for all four chars. Wang et al. [41] however, did not find a concrete correlation between the alkali index and gasification reactivity while studying six different biochars. The author rather found relation between the gasification reactivity and the raman spectra of the respective chars. Numerous other studies based on the above discussed themes have been performed by different authors using the TGA.

Table 2.5 displays a brief review about the kinetic parameters obtained in literature for gasification of diverse chars using different state of the art instruments discussed above. For biomass based chars, activation energy for CO_2 gasification varied in the range from 93.9-251 kJ/mol.

Char source	Gasification agent	Kinetic model	T (^0C)	Particle size	A_0	E_A (kJ/mol)	Apparatus	Ref
Switch grass	H_2O	RPM	1000 - 1100	1 cm	$2.51 \cdot 10^3\, bar^{-1}\, s^{-1}$	112.6	Fixed bed	[55]
Pinewood	CO_2	VM, SCM, RPM	727 - 897	$\leq 3350\,\mu m$	$VM = 4.87 \cdot 10^7\, s^{-1}$ $SCM = 4.43 \cdot 10^4\, s^{-1}$ $RPM = 1.48 \cdot 10^2\, s^{-1}$	$VM = 217$ $SCM = 286$ $RPM = 125$	Fixed bed	[50]
Spent tyre	CO_2	VM, SCM, RPM	750 - 1050	$\leq 150\,\mu m$	$VM = 6.24 \cdot 10^{-4}\, s^{-1}$ $SCM = 6.4 \cdot 10^{-7}\, s^{-1}$ $RPM = 2 \cdot 10^{-5}\, s^{-1}$	$VM = 112.4$ $SCM = 154$ $RPM = 64$	Fixed bed	[42]
Dried sewage sludge	CO_2, H_2O	Emperical	800 - 900	$1.2 - 4.5\,mm$	$CO_2 = 6.3{\cdot}10^4\, bar^{-n}\, s^{-1}$ $H_2O = 3.9{\cdot}10^5\, bar^{-n}\, s^{-1}$	$CO_2 = 163.5$ $H_2O = 171.0$	Fluidized bed	[57]
Shenhua bituminous coal	H_2O	RPM	800 - 1000	$60\,\mu m$	$9.85 \cdot 10^8\, s^{-1}$	267	Fluidized bed	[51]
Zhundong subbituminous coal	H_2O	RPM	800 - 1000	$60\,\mu m$	$1.21 \cdot 10^6\, s^{-1}$	196.4	Fluidized bed	[51]
Beech stick	H_2O	SCM	700 - 850	$6\,mm$	$5.86\, mol\, m^{-2}\, Pa^{-n}\, s^{-1}$	122.88	Fluidized bed	[39]
Indonesian sub-bituminous coal	CO_2	SCM	900 - 1100	$45 - 65\,\mu m$	$174.1\, s^{-1}$	144	DTF	[62]
Japanese cedar	CO_2, H_2O	RPM	900 - 1200	$50 - 100\,\mu m$	$CO_2 = 2.2 \cdot 10^3\, s^{-1}$ $H_2O = 9.9 \cdot 10^4\, s^{-1}$	$CO_2 = 93.9$ $H_2O = 136$	DTF	[64]
Hearth furnace coke	CO_2	RPM	900 - 1050	$63 - 200\,\mu m$	$3.26 \cdot 10^5\, bar^{-n}\, s^{-1}$	162	DTF	[66]

Table continues on the next page

Char source	Gasification agent	Kinetic model	T (^0C)	Particle size	A_0	E_A (kJ/mol)	Apparatus	Ref
Petroleum coke	CO_2	RPM	900 - 975	$\leq 90\,\mu m$	$1.3 \cdot 10^8\, bar^{-n}\, s^{-1}$	260	TGA	[49]
Pelletized wood	CO_2	RPM	800 - 1300	$0.5 - 10\,\mu m$	$1.3 \cdot 10^7 - 4.58 \cdot 10^8\, s^{-1}$	216-251	TGA	[47]
Miscanthus	CO_2	RPM	800 - 1300	$0.5 - 10\,\mu m$	$1.4 \cdot 10^5 - 1.83 \cdot 10^8\, s^{-1}$	177-197	TGA	[47]
Straw	CO_2	RPM	800 - 1300	$0.5 - 10\,\mu m$	$2.15 \cdot 10^4 - 6.82 \cdot 10^4\, s^{-1}$	159-170	TGA	[47]
Peanut shell	CO_2	VM, SCM, RPM	1200 (diff heating rates)	$\leq 74\,\mu m$	$VM = 2.72 \cdot 10^7\, min^{-1}$ $SCM = 7.1 \cdot 10^5\, min^{-1}$ $RPM = 4.01 \cdot 10^6\, min^{-1}$	$VM = 255.2$ $SCM = 232.8$ $RPM = 238.6$	TGA	[70]
Morwell coal	CO_2	RPM	650 - 1100	$90 - 106\,\mu m$	$1.69 \cdot 10^5\, s^{-1}$	168.98	TGA	[71]
Wheat straw	CO_2	RPM, MRPM	900 - 1000	$\leq 74\,\mu m$	$RPM = 7.26 \cdot 10^3\, s^{-1}$ $MRPM = 5.12 \cdot 10^3\, s^{-1}$	$RPM = 163.3$ $MRPM = 153.2$	TGA	[41]
Rice Lemma	CO_2	RPM, MRPM	900 - 1000	$\leq 74\,\mu m$	$RPM = 4.05 \cdot 10^3\, s^{-1}$ $MRPM = 4.07 \cdot 10^3\, s^{-1}$	$RPM = 180.3$ $MRPM = 149.5$	TGA	[41]
Jackfruit leaves	CO_2	VM, SCM, RPM	700 - 950	$90 - 150\,\mu m$	$VM = 2.7 \cdot 10^8\, min^{-1}$ $SCM = 2.5 \cdot 10^8\, min^{-1}$ $RPM = 4.3 \cdot 10^8\, min^{-1}$	$VM = 210 \pm 2$ $SCM = 210 \pm 2$ $RPM = 210 \pm 6$	TGA	[69]
Mango leaves	CO_2	VM, SCM, RPM	700 - 950	$90 - 150\,\mu m$	$VM = 7.9 \cdot 10^8\, min^{-1}$ $SCM = 6.6 \cdot 10^8\, min^{-1}$ $RPM = 7.6 \cdot 10^8\, min^{-1}$	$VM = 217 \pm 2$ $SCM = 218 \pm 2$ $RPM = 216 \pm 5$	TGA	[69]

Table 2.5: Review of kinetic parameters of gasification of diverse chars using different state of the art instruments

2.5 Diffusional limitations within the TGA

2.5.1 Problem Statement

High sensitivity regarding the weight measurement of the samples is an attractive feature of the TGA, which makes it the go to instrument for the researchers to study char gasification kinetics. However, the TGA itself has certain drawbacks which are not considered while determining kinetics of char gasification. A typical example of the TGA crucible containing the char particles is shown in the fig. 2.2 where the reactive gas flows across the crucible mouth. Some TGAs also have a vertical setup where the gas directly flows into the crucible mouth. But irrespective of the setup, the reactive gas is hard to flow through the sample surface, therefore a stagnant gas region exists between the the mouth of the crucible and the upper surface of the sample [59]. Due to this setup, the transport of CO_2 from the mouth of the crucible to the char particle surface is limited by the external diffusion of the gas and then by diffusion within the void spaces [72]. Authors often disregard these diffusion limitations while calculating kinetics or avoid them by increasing gas flow rate until no influence on the measured rate is observed. However this method is not reliable, if the char bed is well below the crucible mouth. Ollero et al. [73] investigated the effects of both the external diffusion and diffusion within the void spaces using different sets of crucible and employed the effectiveness factor technique to quantify their effects. The author showed that, even for temperatures as low as $800\,^0C$, the effectiveness factor was around 0.7 hence emphasizing the importance of taking these effects into consideration while studying kinetics using TGA.

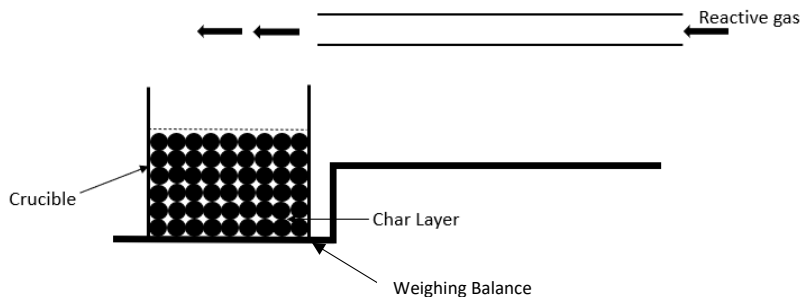

Figure 2.2: A typical description of a TGA crucible containing the char sample

When the reaction is kinetically controlled, bulk gas conditions exist at the reactive surface as well as within the pores of the particle [74]. Schulze et al. [75] used CFD simulations to simulate the gasification of char particles in a TGA and found that in a vertical TGA, CO_2 concentration at the bottom of the crucible fell to about .57 for the bulk concentration of 0.99, thus confirming the fact that diffusion within the empty space above the char sample and within the void spaces of the sample effect the gasification rate. While controlling the reaction temperature and reducing the particle size may eliminate the effects of pore diffusion within the char particle, diffusion within the void spaces of char sample may still considerably effect the reaction rate. Therefore it is necessary to incorporate these effects into the studies regarding gasification kinetics.

2.5.2 Solution proposed

Schulze et al. [75] developed a 0-dimensional numerical model for gasification of char in a TGA and successfully validated it using CFD simulations. This model formed the basis of work presented in chapter 3 of this thesis. The model presented by the author was only applicable for non-porous char particles and did not take into account the effects of pore diffusion on kinetic parameters. Therefore, a detailed kinetic model of char gasification in a TGA is developed and implemented in chapter 3 of this thesis which takes into account the effects diffusion of gas within the empty space of the crucible, diffusion of gas within the void spaces of the char sample and diffusion of gas

within the pores of a char particle. Key features of the model proposed in chapter 3 are as follows:

- The model is first formulated for non-porous reactive char particles similar to the one proposed by Schulze et al. [75].
- The model is then validated using 3-D particle simulations performed by Schulze et al. [75] based on its steady state solutions.
- After validation, the model is then extended to the porous particles and takes into the account pore diffusion limitations within the char sample. RPM model is used to predict the evolution of char porous structure with conversion.
- In order to implement the model, isothermal CO_2 gasification experiments of biochar are performed using a TGA. A detailed experimental scheme is discussed in chapter 2 of this thesis. The kinetic parameters are then obtained using the RPM model as discussed in section 1.3.
- The parameters are then inputed into the model to take into account the different diffusional resistances discussed in our problem statement.
- New and refined kinetic parameters are then obtained by comparing and tuning model-predicted results with the experimental results.

2.6 Synergistic effects between co-fed biomass and plastics during their thermo-chemical conversion

2.6.1 Background

Biomass's promising energy potential which can be tapped using thermo-chemical conversion routes has been discussed in the previous sections. Pyrolysis and gasification

in particular have attracted much interest from researchers worldwide due to their ability to use biomass to produce multi-purpose fuels. However one major concern associated with the fuels especially bio-oil obtained using pyrolysis of biomass is its low calorific value and high oxygen content, which makes it unstable and requires considerable upgradation before it can be used as a proper fuel [76]. According to Xiong et al. [77] depending upon the fuel type, oxygen content in the pyrolysis oil can range from 35-50 % resulting in its corrosion and instability. To upgrade the quality of bio-oil, two main pathways exist [76]: high-pressure hydrogenation processing and catalytic cracking and co-pyrolysis of biomass with hydrogen-rich feedstock such as plastics. The second pathway i.e co-feeding of biomass and plastics has gained interest among researchers due to its simplicity and safe operation under ambient pressure. It not only helps to improve the quantity of bio-oil produced but also upgrades its quality using synergistic effects which have later been discussed in detail.

Plastics have become a basic support material of our modern day lives and their excessive usage is posing massive environmental challenges regarding its disposal. Therefore their thermo-chemical conversion is viewed as a possible approach to manage waste plastics with the added benefit of energy recovery. Direct gasification of plastics faces challenges such as high tar content in syngas and agglomeration of particles in fluidized bed reactors [78]. Therefore co-feeding with biomass is considered as a more flexible option for thermally utilizing plastics as energy generating fuels. Plastics are synthetic polymers of hydrocarbons derived mostly from fossil fuels. Major elemental constituents of plastics are carbon and hydrogen with hydrogen weight percent reaching as high as 14% for plastics like polyethylene and polystyrene. Thus, co-feeding biomass and plastics upgrade the quality of its products, by balancing the C, H and O mass ratios in the feedstock.

2.6.2 Review on observed synergistic effects by co-pyrolysing biomass and plastics

To understand synergistic effects between biomass and plastics, knowledge of their individual pyrolysis reaction mechanism is essential. Biomass degradation is characterized by a series of complex exothermic and endothermic reactions involving ionic/non-ionic reactions whereas pyrolysis of plastics occur through a radical mechanism involving chain initiation, propagation and termination steps [79]. When co-pyrolysed, both biomass and plastics have similar temeprature ranges for their respective degradation which overlap each other. While the biomass degradation starts at around $200\,^0C$ and may continue upto temperatures greater than $700\,^0C$ depending upon its composition, plastics degrade in a narrow range of temperature ranging between $350 - 700\,^0C$. This overlap of temperature range for degradation causes interactions between the two reaction mechanisms and their intermediates thus causing synergies which effect the products obtained from pyrolysis, especially bio-oil [80].

A possible reaction mechanism for synergies between the two feedstocks has been provided in literature as follows ([79], [81], [82]): As the reaction temperature increases, plastics melt and coat the biomass surface. Therefore, when initial intermediates and volatiles from biomass are produced, they are unable to escape this coating. Therefore, lots of radicals are formed from decomposition of cellulose. These radicals then initiate the scissoring of plastic polymer chain to form radicals. Plastics have higher hydrogen content, therefore producing a large quantity of hydrogen radicals which are then abstracted by the intermediates from biomass degradation in a process known as hydrogen transfer effect, thus stablizing the primary products from cellulose decomposition and improving their hydrogen quantity. This inhibits the free radical polymerization of biomass intermediates thus increasing the quantity of lighter hydrocarbons and volatiles and reducing the char content. Hydrocarbon radicals from plastics also catalyze the degradation of lignin thus further reducing the char content and increasing the quantity of volatiles. Therefore, two major synergistic effects of co-pyrolyzing biomass and plas-

tics are: (i) Increase in H/C ratio of the bio-oil (ii) Increase in the quantity of bio-oil and volatiles followed by a decrease in the char formation. The only exception observed against these findings is when Polyvinyl Chloride (PVC) is the plastic utilized. In this case it is mostly observed that upon pyrolysis, solid residue actually increases. This is usually reasoned with the fact that HCl evolved from PVC dehydrates the cellulose and inhibits the de-polymerization reactions [80]. Most of the literature studies published on the topic concur with these results. A review on a few of such studies is explored next.

Xiong et al. [77] investigated co-pyrolysis of HDPE and potato blends using a TGA and a tubular furnace. The H/C ratio of bio-oil increased from 1.29 to 2 as the HDPE weight percent was increased to 50, thus confirming the above discussed synergistic effects. Similar results were also reported by Lu. et al. [80] upon co-pyrolysis of pinewood and polyethylene (PE). Upon increasing the content of PE within the feedstock, bio-oil quantity and the char quantity increased and decreased respectively. The blends of PE also increased the total surface area of the char and decreased its H/C ratio thus making it more stable. Chen et al. [81] found that when Paulownia Wood (PAW) was co-pyrolyzed with different plastics (PP, PVC and PET), more volatiles were released than the predicted value and the mean activation energy declined upon blending the biomass with plastics. The author also studied morphology of the chars produced using SEM analysis. Burra et al. [83] observed synergies during co-pyrolysis of pinewood and different plastics using a TGA and quantified it by studying its kinetics using distributed activation energy model (DAEM). Upon investing kinetics using Coats-Redfern method, Salvilla et al. [84] reported that activation energy of plastics during co-pyrolysis with biomass was lower than the activation energy observed during their individual pyrolysis. However, there was no effect on the activation energy of the biomass. This was also backed by Chen et al. [85] as the author reported that activation energies of different plastics were significantly reduced when co-pyrolyzed with microalgae. Solid residue amounts also decrease upon co-pyrolysis with PVC acting as a expection for reasons discussed above.

2.6.3 Evaluation of synergistic effects on char reactivity

Literature published on synergistic effects between biomass and plastics clearly preview the positive effects that co-pyrolysing both these feedstocks have on bio-oil in terms of its increased yield and improved quality. It is also well known that the char yield decreases upon co-pyrolysis. However, it is scarcely published how the char reactivity is effected by co-pyrolysing biomass and plastics. Questions arise as to how the gasification characteristics of char change when they are produced in this manner. Most authors have only conducted char morphology analysis using SEM analysis ([80], [81]). The only significant and relatable work is published by Wang et al. [86] wherein the author observed synergistic effects of co-pyrolysis of biomass and polyurethane and then studied the oxidation reactivity of the char formed. Upon co-pyrolysis with plastic, the char formed showed higher heating values and char oxidation is thus promoted. Co-gasification of biomass and plastics have shown to improve syngas yield, hydrogen yield and energy yield of the syngas thus suggesting that the char reactivity may be enhanced when co-pyrolysis is used ([87], [88]). However concrete evidence regarding this is lacking and therefore chapter 4 in this thesis attempts to address the same.

Pyrolysis characteristics of softwood(SW) and High Density Polyethylene(HDPE) are first studied using a TGA and an attempt is made to quantify the synergistic effects observed. Then using different blend ratios, char is formed in a tubular furnace and its gasification reactivity is studied in CO_2 atmosphere using the TGA. A Similar approach to the one discussed in chapter 3 is employed to determine the kinetic parameters related to char gasification and summarize the effects of co-pyrolysis on char reactivity. A detailed experimentation of the scheme is laid out in chapter 2.

Chapter 3

Experimental Techniques

3.1 Experimental study for the char gasification using the TGA

3.1.1 Char source

Biochar used for this model's study, was obtained from the Thermo-catalytic reforming (TCR) of softwood pellets. All the TCR experiments were conducted by M.K. Gill during her research activity at University of Alberta. A detailed description of the experimental setup and methodology used in performing TCR experiments is laid out in her master's thesis [89]. Softwood pellets of the size 6-8 mm in diameter and a length of 20-30 mm were pyrolysed using a lab scale TCR in N_2 atmosphere. Different experiments were performed by Manjot at different reactor and reformer temperatures. The char used for this study was produced at reactor temperature of $450\,^0C$ and a reformer temperature of $600\,^0C$. Figure 3.1 shows the char obtained from TCR of softwood pellets. The char obtained was grinded to powdered form using a coffee grinder and then segregated using meshes between particle size 190-205 μm. The char was then dried for 24 hours in an oven and sealed in airtight plastic bags for further analysis.

Figure 3.1: Char production from TCR of softwood pellets

3.1.2 Char characterization

Proximate Analysis

Proximate analysis to determine the moisture, volatile, fixed carbon and ash content of the biochar sample, was performed using LECO TGA 701 instrument (Fig. 2.1) following ASTM D7582 methodology. Approximately 1g of the sample was placed in a ceramic crucible for analysis. The TGA was then heated from the room temperature to $107\,^0C$ at $20\,^0C$/min in nitogen atmosphere and isothermal conditions were maintained untill there was no further mass loss recorded. The total mass loss uptill that point accounted for the moisture content in the sample. Next, the volatiles in the sample were calculated by heating the TGA to $900\,^0C$ at the rate of $40\,^0C$/min and holding the temperature constant for 15 min under the nitrogen atmosphere. The ash content was then measured by lowering the temperature to $500\,^0C$ followed by heating uptill $575 \pm 25\,^0C$ under oxygen environment. Lastly, the fixed carbon percentage in the sample was calculated by subtracting sum of percentages of moisture content, volatile content and ash content from 100.

Figure 3.2: LECO TGA 701

Elemental Analysis

Elemental composition of the biochar was determined using a Thermo fisher flash 2000 organic elemental analyzer (Fig. 3.3) at the Analytical and Instrumentation Laboratory of the Chemistry Department, University of Alberta. The tin cup enclosing the sample was dropped in the vertical quartz tube which is maintained at a temperature of $1000\,^0C$ with a constant flow of helium as a carrier gas. In the combustion chamber, a fixed volume of oxygen gas is then mixed with the helium for combustion of sample and tin cup. The peaks for Carbon, Hydrogen, Nitrogen and Sulphur are predicted by the Eager Xperience software based on their thermal conductivity. The oxygen weight percent is then determined by the composition balance.

Figure 3.3: Thermo fisher FLASH 2000 instrument

BET surface area study

To obtain the specific surface area of the char, Brunauer-Emmett-Teller (BET) experiments were performed using an Autosorb IQ instrument (Fig. 3.4) manufactured by Quantachrome instruments. 9 mm cells were filled with the sample till 3/4th of the cell (bulb) volume and were then degassed by heating the sample in vacuum at $250\,^0C$ at a heating rate of $5\,^0C$/min and a soak time of 4 hours. The adsorption and desorption isotherms of nitrogen were measured at a relative pressure range of 0-0.99 at 77 K. The multipoint BET surface areas were measured at a relative pressure range of 0.05-0.35 (unit).

Figure 3.4: BET set-up

3.1.3 TGA gasification experiments

To obtain the kinetic parameters of the boudouard reaction, gasification experiments with CO_2 were carried out using the thermogravimetric analyser *SDT Q600* (Fig. 3.5) manufactured by TA instruments (New Castle, DE, USA). It uses a horizontal dual beam design with a balance sensitivity of 0.1 μg to analyze the weight of the sample. The horizontal furnace enclosed in perforated stainless steel allows the TGA to operate at temperatures upto $1500\,^0C$. An alumina crucible of diameter 5.5 mm and 3.3 mm in height is used as a sample holder. Isothermal gasification experiments were conducted at three different temperatures: $800\,^0C$, $850\,^0C$ and $900\,^0C$. About 25 mg of the biochar sample was placed in the alumina crucible. The TGA was then heated from the ambient temperature to the desired temperature at a heating rate of $20\,^0C$/min under the inert atmosphere of N_2. The gas was then subsequently switched to pure CO_2 at a flowrate of 100 ml/min once the desired temperature was achieved. Isothermal conditions were

maintained until there was no further mass loss recorded. For each gasification temperature, three experimental runs were carried out to have desired accuracy. The data retrieved from the instrument was analyzed using TA instruments Universal Analysis 2000 software.

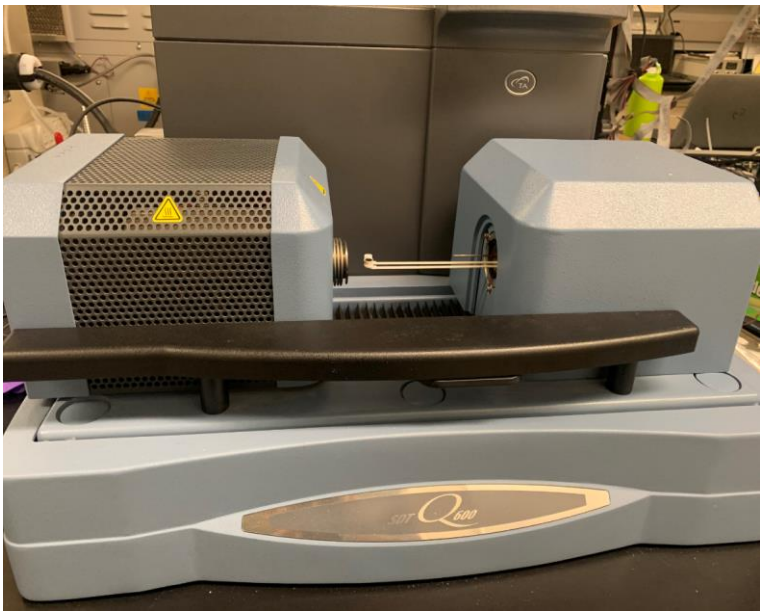

Figure 3.5: SDT Q600 TGA set-up

3.2 Experimental study for the blends of SW and HDPE

3.2.1 Feedstock preparation and its characterization

In order to study the synergistic effects between biomass and plastics, Softwood(SW) and High Density Polyethylene (HDPE) were chosen as the feedstock. The SW pellets were supplied by Vanderwell Contractors in Slave Lake, Alberta and had a diameter of 6-8 mm and a length of 20-30 mm. These pellets were crushed using a coffee grinder and then segregated for particle sizes less than 200 μm using meshes. The particles were dried in an oven for 24 hrs and then sealed in airtight bags. The HDPE used was

in powdered form with a particle size less than 200 μm

Proximate analysis and elemental analysis of the prepared feedstocks were conducted according to methodology discussed in section 2.1.2. An additional analysis of SW particles was performed using scanning electron microscopy (SEM), which has been discussed in detail in section 2.2.3.

3.2.2 TGA Pyrolysis characterization experiments

To evaluate synergistic effects quantitatively, co-pyrolysis of different blends of the feedstock were performed using thermogravimetric analyser *SDT Q600* (Fig. 3.5). Samples of SW and HDPE with HDPE weight ratio 0, 0.25, 0.5, 0.75, 1 were prepared using a mixer to achieve homogeneity. Blends with ratio 0 and 1 correspond to pure biomass and pure plastic samples respectively. To obtain pyrolysis characteristics of these blends, approximately 10 mg of each sample was introduced into the TGA crucible. The sample was then heated from room temperature to $700\,^0C$ at a heating rate of 20 ^0C/min in a nitrogen flow rate of 100 ml. Each set of experiment was repeated 3 time to achieve desired accuracy. The data retrieved from the instrument was analyzed using TA instruments Universal Analysis 2000 software.

3.2.3 Char formation using a tubular furnace and its characterization

Char formation

The char remaining at the end of TGA experiments is quite less for it to be used for further characterization and expeiments. Therefore in order to make char from the mixture blends, a Thermolyne 79300 tubular furnace (Fig. 3.6) was used. The furnace chamber comprises of a mullite tube with dimensions of 5.9 cm diameter and 80 cm length. Metallic coils embeded in a rigid refractory material are used to heat the chamber. The furnace temperature is monitored by a K-type thermocouple and the

temperature can be controlled using the control unit located below the furnace. Heat losses from the tube were minimized by insulating the ends of the tube using a K-wool and fibrefax materials. Cole-Parmer rotameter was used to regulate the flow rate. For char formation, 2 gm of samples containing blends with plastic weight ratio 0, 0.25, 0.5 and 0.75 were taken in crucibles and placed inside the tube. The tube was then purged with Nitrogen gas at 30 ml/sec for 15 mins to remove any air present within the tube. Increasing the Nitrogen flow rate to 50 ml/sec, temeprature was increased from room temeprature to $700\,^0C$ at a heating rate of $20\,^0C/min$. The temperature was maintained at $700\,^0C$ for 20 mins and then cooled down to room temperature under the maintained Nitrogen flow rate. Total 4 experiments were conducted to reproduce accuracy and have significant char for further experiments. The char was collected and sealed in airtight bags.

Figure 3.6: Thermolyne 79300 tube furnace

Additional Char characterization:SEM analysis

Apart from the char characterization techniques described in section 2.1.2, char from different blends of SW and HDPE mixtures was also subjected to Scanning Electron Microscopy (SEM) analysis to understand its structural morphology. The analsysis was performed on Zeiss Sigma 300 VP-FESEM (Fig. 3.7) at the Department of Earth and Atmospheric Sciences, University of Alberta. Conductive carbon tape was used to ground the sample to the holder. For analysis, SEM scans were conducted at an accelerating voltage of 10 kV.

Figure 3.7: Zeiss Sigma 300 VP-FESEM

3.2.4 TGA gasification experiments

To asses the reactivity of chars formed from different blends of SW and HDPE mixtures, similar experiments as discussed in section 2.1.3 were performed in the TGA (Fig. 3.5). Isothermal gasification experiments were conducted at three different temperatures: $800\,^0C$, $850\,^0C$ and $900\,^0C$. About 10 mg of the biochar sample was placed in the alumina crucible. The TGA was then heated from the ambient temperature to the

desired temperature at a heating rate of $20\,^0C$/min under the inert atmosphere of N_2. The gas was then subsequently switched to pure CO_2 at a flowrate of 100 ml/min once the desired temperature was achieved. Isothermal conditions were maintained until there was no further mass loss recorded. For each gasification temperature, three experimental runs were carried out to have desired accuracy. The data retrieved from the instrument was analyzed using TA instruments Universal Analysis 2000 software.

Chapter 4

Numerical modeling of TGA:Model formulation,Validation and Solution methodology

4.1 Model formulation

In the previous study conducted by the Schulze et al. [75], macroscopic 3-D simulation of the TGA was performed to get insight into the phenomenon occurring within the crucible. Using Peclet numbers, it was analysed that the convection induced by the inlet gas flow plays a minor role in the heat and mass transfer phenomenons compared to diffusion. Simulation also illustrated that major mass transfer resistance occurred within the crucible and hence the presented model captures the phenomenon within the TGA crucible. The model follows the 0-dimensional approach with the assumption of the *Lumped Capacitance Method* which assumes that temperature and species mass fraction is spatially uniform within the sample during the transient process. The variables defined in the model are presented in the fig 4.1 . Here h is the char sample height, H is the height of crucible and D is the diameter of the crucible. The subscript ∞ denotes the bulk or inlet gas conditions, s denotes the sample surface, pm denotes

the porous media i.e the sample and w refers to the crucible wall.

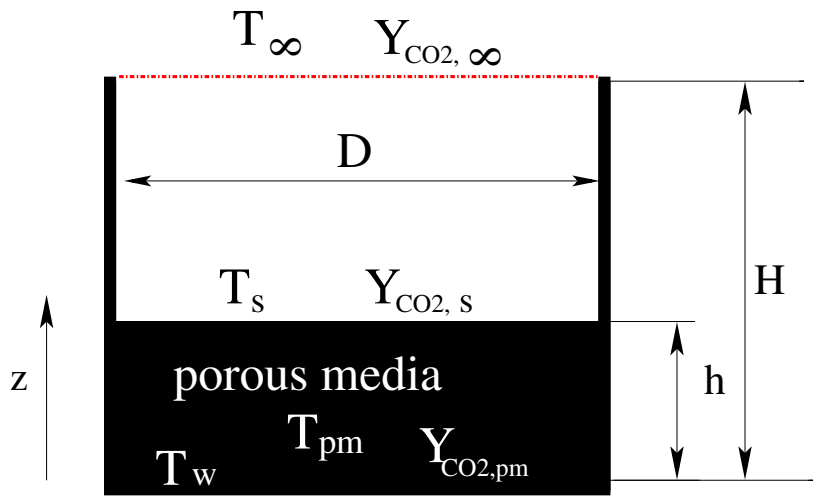

Figure 4.1: Schematic distribution of temperature and species mass fraction within the crucible

The heat transport phenomenons occurring within the crucible are heat conduction and radiation from the bulk gas towards the surface of the char layer, conduction between the crucible wall and the porous media and consumption of heat from the endothermic boudouard reaction. For the species transport, diffusion, heterogeneous reaction and the stefan flow generated due this reaction are the mass transfer phenomenons accounted for. For validation of the model, the particles are assumed to be non-porous and the reaction is taking place on the particle surface only. During the chemical reaction, radius of the char particle r_p and height of the sample h will decrease as the reaction proceeds but for validation of the model against the previous published work[75], steady state equations of the proposed model are solved and therefore for validation, h and r_p are assumed to be constant. After validation, an extension of the model to porous particles is presented wherein these changes in particle radius and sample height are accounted for. Based on the current assumptions, the detailed model is formulated as shown below.

4.2 0-D model for reacting non-porous particles

Reacting surface for non-porous particles

Number of particles in the TGA sample is given by N_p and can be calculated as:

$$N_p = \frac{V(1-\varepsilon)}{V_p} = \frac{3}{4}\frac{R_{TGA}^2 h}{r_p^3} \tag{4.1}$$

here $R_{TGA} = \frac{D}{2}$ is the radius of the TGA crucible, $V = \pi\, R_{TGA}^2\, h$ is the sample volume, ε is the bed porosity and $V_p = \frac{4}{3}\,\pi\, r_p^3$ is the volume of a single particle.

The total surface area of particles participating in the reaction is

$$\sum S_p = N_p S_p = \frac{V(1-\varepsilon)S_p}{V_p} = 3\pi\frac{R_{TGA}^2 h}{r_p} \tag{4.2}$$

where S_p is the surface area of a single particle.

Energy conservation

The temperature of porous media T_{pm} is calculated by solving transport equations of heat fluxes from conduction, radiation and heat of reaction as follows:

$$V\left(\rho_g\,\varepsilon\,c_{p,g} \;+\; \rho_s\,(1-\varepsilon)\,c_s\right)\frac{dT_{pm}}{dt} = \dot{Q}_{Wall} + \dot{Q}_{Gas} + \dot{Q}_{Reaction} \tag{4.3}$$

here ρ_g and $c_{p,g}$ are respectively the density and heat capacity of the gas within the voids of the sample. Similarly, ρ_s and c_s are the density and heat capacity of solid char particles. $\dot{Q}_{Wall}$ is the conductive heat flux between the crucible wall and the sample, $\dot{Q}_{Gas}$ is the heat flux conducted from the bulk gas to the surface of the sample and then from the surface to within the sample. $\dot{Q}_{Reaction}$ is the heat flux accounting for the endothermic reaction.

Heat flux from wall can be written as:

$$\dot{Q}_{Wall} = \lambda_{eff}\frac{A}{h/2}\,(T_w - T_{pm}) \tag{4.4}$$

λ_{eff} is the effective conductivity within the porous media and $A = \pi\, R_{TGA}^2$.

Heat flux due to the reaction can be written as:

$$\dot{Q}_{Reaction} = \left(\sum \dot{m}_C\right) \Delta_R H \tag{4.5}$$

where $(\sum \dot{m}_C)$ is overall carbon mass flow for all particles inside the porous media zone and is defined later in species transport section. $\Delta_R H$ is the heat of reaction.

For the heat flow from the bulk gas, a series of heat resistances are considered, namely conduction and radiation through the gas to the surface and then this is conducted from the surface to the porous media.

Balance Interface-Char Layer

$$\dot{Q}_{Gas} = \lambda_{eff} \frac{A}{h/2} \left(T_S - T_{pm}\right) \tag{4.6}$$

Balance Ambient gas-Interface

$$\dot{Q}_{Gas} = \lambda_g \frac{A}{H-h} \left(T_\infty - T_S\right) + A\, \varepsilon_{emissivity}\, \sigma_{SB}\, \left(T_\infty^4 - T_S^4\right) \tag{4.7}$$

λ_g is heat conductivity of gas within the top of the crucible and the sample surface. $\varepsilon_{emissivity}$ is the particle emissivity and σ_{SB} is the Stefan-Boltzmann constant.

CO_2 species balance for the gas phase inside porous media

The species transport balance within the crucible to calculate CO_2 mass fraction within the porous media is written as follows:

$$\varepsilon\, V\, \rho_g \frac{dY_{CO_2,pm}}{dt} = \underbrace{(A\varepsilon)\, \frac{D_{eff}}{h}\, \rho_g\, \left(Y_{CO_2,S} - Y_{CO_2,pm}\right)}_{Diffusion\, from\, surface} - \underbrace{k \sum S_p\, \rho_g\, Y_{CO_2,pm}}_{Reaction}$$

$$\underbrace{-\left(\sum S_p\right)\dot{m}''_C\,Y_{CO_2,pm}}_{Convection:\,Stefan\,Flow} \tag{4.8}$$

The mass transfer phenomena occurring within the crucible as represented by the underbraces are diffusion from the surface, consumption due to reaction and Stefan flow. $\dot{m}''_C$ is the carbon mass flux for a single particle and $\sum S_p \dot{m}''_C$ is the total carbon mass flow earlier also represented by $(\sum \dot{m}_C)$. εV is the volume of gas phase inside the porous media, D_{eff} is the effective diffusion coefficient within porous media, D_g is the diffusion coefficient of gas between crucible top and sample surface and k is the reaction kinetic constant.

Carbon mass flux for a single reacting particle is defined by Turns [90].

$$\dot{m}''_C = k\,\frac{MW_C}{MW_{CO_2}}\,\rho_g\,Y_{CO2,pm} \tag{4.9}$$

Balance Ambient gas-Interface

Similar to the heat transport, diffusion from bulk to char surface is transmitted from surface to porous media and species balance at char surface can be written as:

$$(A\varepsilon)\frac{D_{eff}}{h}\,\rho_g\,(Y_{CO_2,S} - Y_{CO_2,pm}) = (A\varepsilon)\frac{D_g}{H-h}\,\rho_g\,(Y_{CO_2,\infty} - Y_{CO_2,S}) - N_p\,\dot{m}_C\,Y_{CO_2,S} \tag{4.10}$$

CO species balance for the gas phase inside porous media

Similarly CO species balance inside porous media and CO balance at char surface is written as:

$$\varepsilon\,V\,\rho_g\,\frac{dY_{CO,pm}}{dt} = \underbrace{(A\varepsilon)\,\frac{D_{eff}}{h}\,\rho_g\,(Y_{CO,S} - Y_{CO,pm})}_{Diffusion\,from\,surface} + \underbrace{2\,\frac{M_{CO}}{M_{CO_2}}\,k\,\sum S_p\,\rho_g\,Y_{CO_2,pm}}_{Reaction}$$

$$\underbrace{-\left(\sum S_p\right)\dot{m}''_C\,Y_{CO,pm}}_{Convection:\,Stefan\,Flow} \tag{4.11}$$

$$(A\varepsilon)\,\frac{D_{eff}}{h}\,\rho_g\,(Y_{CO,S} - Y_{CO,pm}) = (A\varepsilon)\,\frac{D_g}{H-h}\,\rho_g\,(Y_{CO,\infty} - Y_{CO,S}) - N_p\,\dot{m}_C\,Y_{CO,S} \tag{4.12}$$

Effective properties

Heat conductivity

The effective heat conductivity for the porous materials can be written as a heat transfer through parallel layers of fluid and solid [91].

$$\lambda_{eff} = (1 - \varepsilon)\,\lambda_s + \varepsilon\,\lambda_g \tag{4.13}$$

Diffusion coefficient

In order to calculate the diffusion coefficient of gases, Lewis number is assumed to be unity as it was demonstrated that Lewis number is unity in large range of temperatures [44]. The diffusion of gases through porous media is reviewed by szekely et al. [35]. However, due to high porosity of the sample, it can be assumed that the voids between the char particles are much larger than the mean free path of the molecules, so that the influence of knudsen diffusivity on the effective diffusion coeffecient can be neglected and effective diffusion scales linear with the void space or bed porosity (ε)

$$D_{eff} = \frac{\varepsilon}{\tau} D_g = \varepsilon^2 D_g \tag{4.14}$$

where D_g is the diffusion coefficient in the bulk gas phase, τ is tortuosity of the porous media. Tortuosity is a property of a curve being tortuous and in this work it has been lumped into $\frac{1}{\varepsilon}$ [44].

To validate the model using CFD simulation performed by Schulze et al. [75] tortousity within the voids of the sample was assumed to be 1 and the following relation was used.

$$D_{eff} = \varepsilon D_g \tag{4.15}$$

Reaction kinetics

For modeling the heterogeneous reaction kinetics, Arrhenius expression is chosen

$$k = A_0 \exp \frac{-E_A}{RT} \tag{4.16}$$

4.3 Validation of 0-D model against 3-D CFD simulations

Validation methodology

Validation of the presented model was carried out by solving steady state versions of the above equations using MATLAB 2019 software and the corresponding results were compared against particle-resolved CFD simulations of a representative section of the gasifying char particles in the crucible. The detailed work on the simulations has been articulated in the research article published in FUEL 2017 journal [75] . Setup of the computational domain and snippets of simulation results as published in the research article are shown in figures 4.2 and 4.3 respectively after permission from Elsevier .
The packed bed comprised of approximately 40 spherical particles. Kinetic parameters for the boudouard reaction were taken from Caram and Amundson [92]. The results illustrated transition from kinetically controlled regime to diffusion controlled regime as the inlet gas temperature increased from 900 K to 1100 K. As seen in fig 4.3, CO_2 mass fraction at the bottom wall decreases to 0.58 for inlet gas concentration of 0.99 as the inlet gas temperature increases to 1100 K, thus suggesting a shift of regimes.

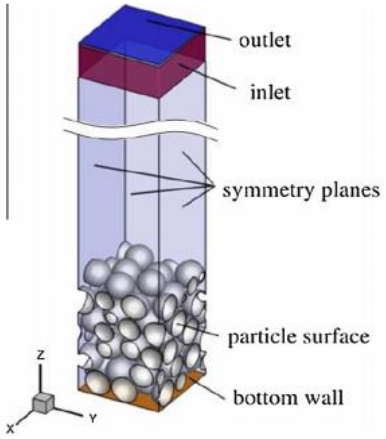

Figure 4.2: Computational domain of particle-resolved simulations adapted with permission from [75]

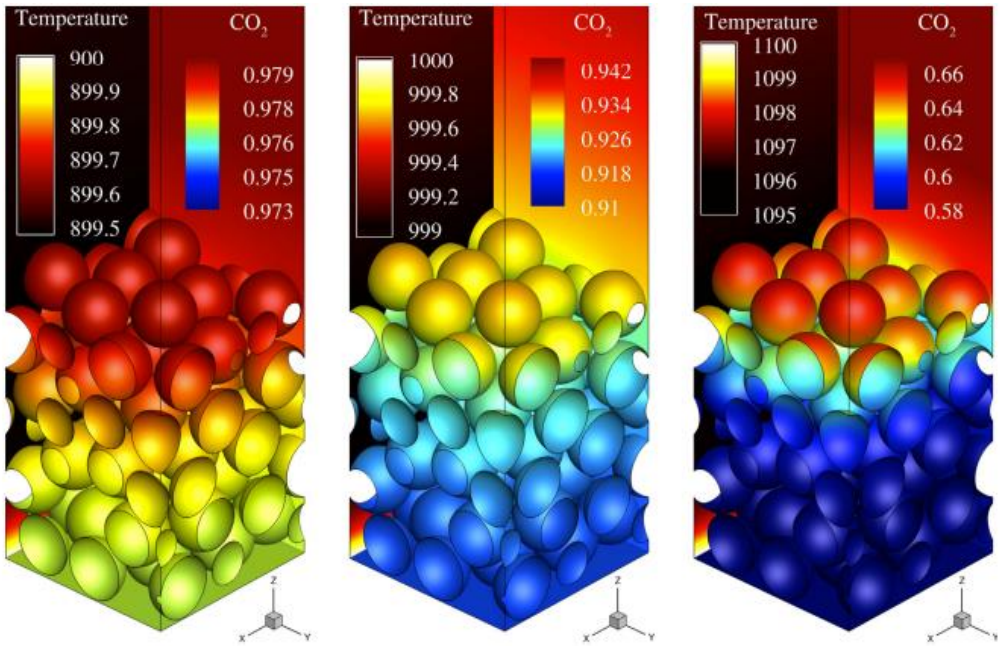

(a) $T_G = 900\,K$ (b) $T_G = 1000\,K$ (c) $T_G = 1100\,K$

Figure 4.3: Temperature and CO_2 mass fraction contours from CFD simulations adapted with permission from [75]

Steady state versions of the equations presented in the 0-d model were solved to validate the model against CFD simulations. Table 4.1 displays numerical values of different properties of char layer, crucible dimensions and kinetic parameters inputted to solve the equations in MATLAB 2019 software.

Implicit scheme was used to solve set of equations iteratively. Different properties such as density, conductivity and heat capacity of gaseous mixture in porous media and surface, were calculated based on CO_2, CO and N_2 mass fractions and updated with each iteration. This ensured that dependence of these properties on temperature was accounted accurately. Iterations were performed until relative error between results of previous iteration and current iteration was less than 10^{-7}. Typically, around 50 iterations were required to reach the solution with desired accuracy.

Table 4.1: Numerical values inputted of different constants in MATLAB software

constant	**Symbol**	**Unit**	**Value**
Crucible height	H	m	10^{-3}
Crucible diameter	D	m	7^{-3}
Sample height	h	m	1.5^{-3}
Particle radius	r_p	m	1.5^{-4}
Void fraction	ε	-	0.5
Char density	ρ_s	kg m^{-3}	1000
Heat capacity of char	c_s	J K^{-1}	1000
Char conductivity	λ_s	W m^{-1} K^{-1}	0.23
Emissivity	$\varepsilon_{emissivity}$	-	1.0
Frequency Factor	A_0	m s^{-1}	4.016*10^8
Activation Energy	E_A	J mol^{-1}	2.477*10^5

Validation results

To validate the model, steady state results of mass fraction of CO_2 in porous media ($Y_{CO_2,pm}$), sample temperature (T_{pm}) and carbon mass flux ($\dot{m}''_C$) were compared against corresponding results from CFD simulations. Inlet gas CO_2 mass fraction ($Y_{CO_2,\infty}$) was set at 0.5 and 0.99, while inlet gas temperature (T_∞) was varied from 900 K to 1200 K for both the cases. Figures 4.4 - 4.7 illustrate these comparisons and it can be verified that, the model-based results and CFD simulation based data are in good agreement with each other. Figures 4.4 and 4.5 compare the results for different bulk temperatures and inlet CO_2 concentration of 0.5 whereas figures 4.6 and 4.7 compare the results at inlet CO_2 concentration of 0.99. For both the cases of inlet CO_2 mass fraction 0.5 and 0.99, as the bulk gas temperature increases, CO_2 mass fraction within the sample decreases thus implying that diffusion within the voids plays an important role. This also indicates a shift from kinetically-controlled regime to diffusion-controlled regime as the bulk temperature increase. Temperature within the porous media is less than the bulk temperature due to the endothermic boudouard reaction and this difference increases as the bulk temperature increases. Carbon mass flux also increases as the temperature increase, because reactivity of char particles increases with increasing temperature.
Maximum relative error between the two data sets is about 7.7 % for $Y_{CO_2,\infty}$=0.5 and T_∞=1200 K (Fig 4.4), which can also be seen for the carbon mass flux curve(Fig 4.5). Apart from this, general correspondence between 0-D model and CFD data set is quite convincing and the model can be verified as correctly devised.

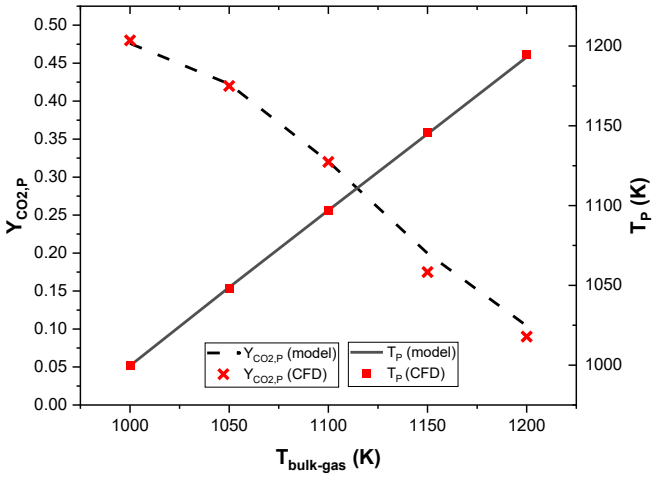

Figure 4.4: Sample Temperature and CO_2 mass fraction in porous media for different inlet gas temperatures and $Y_{CO_2,\infty}$=0.5

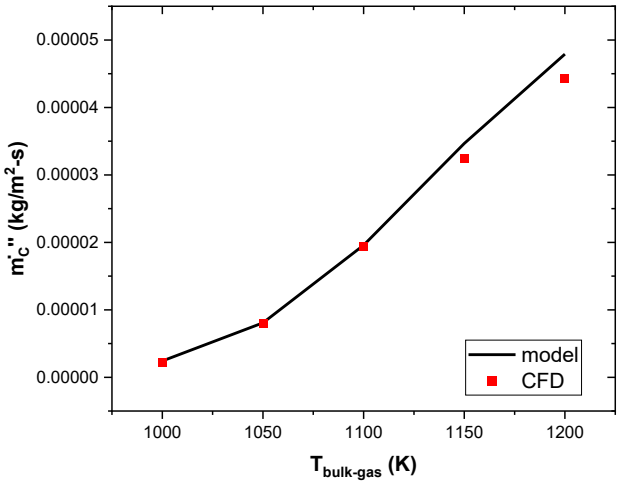

Figure 4.5: Carbon mass flux for different inlet gas temperatures and $Y_{CO_2,\infty}$=0.5

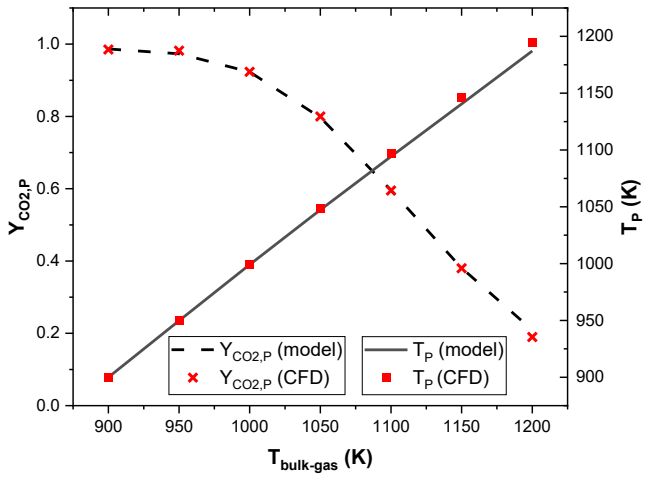

Figure 4.6: Sample Temperature and CO_2 mass fraction in porous media for different inlet gas temperatures and $Y_{CO_2,\infty}$=0.99

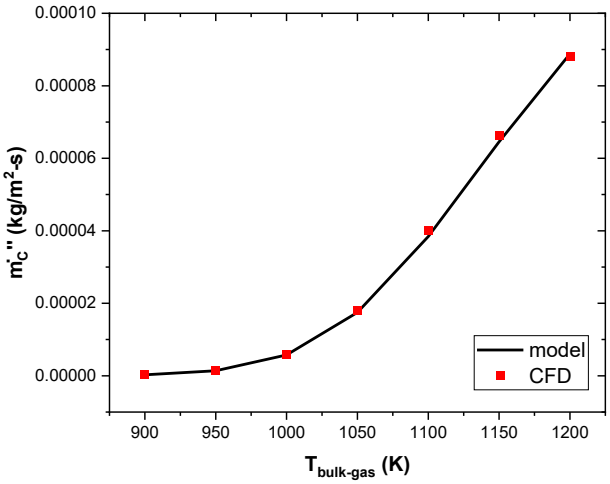

Figure 4.7: Carbon mass flux for different inlet gas temperatures and $Y_{CO_2,\infty}$=0.99

4.4 Extension of model to porous particles

After validation of the 0-d model for the non porous particles, the model can now be extended to the porous particles and take into account particle radius and sample height change as the reaction proceeds. A single porous particle inside the sample is as shown in fig. 4.8. For porous particles, reaction will now take place at the particle surface as well as within the pores. As a result, char particle radius and height of sample will decrease thus decreasing the mass of the sample as the reaction proceeds. Particle porosity will increase with time because reaction inside the pores will cause pores to overlap each other [93].

With the reaction taking place inside the pores, mass fraction of CO_2, CO and N_2 inside the pores is represented with subscript pp. Mass transfer on the surface of particles is omitted and it is assumed that $Y_{CO_2,pm}$=$Y_{CO_2,sp}$. Temperature of the whole sample is constant at any particular time and is represented again as T_{pm}.

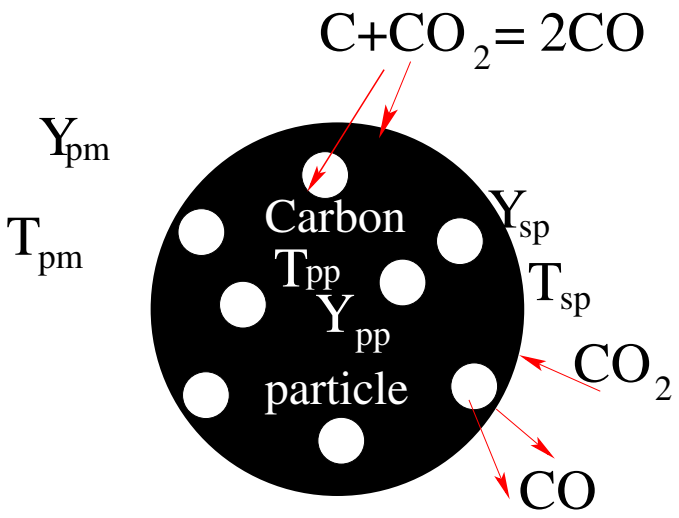

Figure 4.8: Porous particle inside the TGA sample

The rate of change of mass of the particle, $\dot{m}_P$ can be mathematically formulated as:

$$\dot{m}_p = \frac{dm_p}{dt} = \underbrace{V_P \frac{d\rho_P}{dt}}_{\dot{m}_{C,V}} + \underbrace{\rho_P \frac{dV_P}{dt}}_{\dot{m}_{C,S}} \tag{4.17}$$

Here, ρ_P is the density of the char particle. The first term on the right side of the Eq. (4.17) characterizes the change in the particle density due to carbon conversion inside the porous particle. The second term defines the decrease in the particle size due to heterogeneous reactions on the particle surface. The density and volume of the char particle can be defined as follows:

$$\rho_P = \rho_{g,P}\ \varepsilon_P + (1-\varepsilon_P)\,\rho_C = \varepsilon_P\,(\rho_{g,P}-\rho_C) + \rho_C, \quad V_P = \frac{4}{3}\pi\, r_P^3 \tag{4.18}$$

where ε_p is the porosity inside the particle, $\rho_{g,P}$ is the density of gas inside the pores and ρ_c is the density of pure carbon. Using Eqns. (4.17) and (4.18) we obtain volumetric-based and surface-based carbon mass flows.

$$\dot{m}_{C,V} = V_P\,\frac{d\rho_P}{dt} = V_P\ (\rho_{g,P}-\rho_C)\,\frac{d\varepsilon_P}{dt} \approx -V_P\,\rho_C\frac{d\varepsilon_P}{dt} \tag{4.19}$$

$$\dot{m}_{C,S} = \rho_P\,\frac{dV_P}{dt} = \rho_P\,\frac{4}{3}\pi\frac{d}{dt}\left(r_P^3\right) \tag{4.20}$$

Using eqs. (4.19) and (4.20) we can calculate the dynamics of the particle porosity and particle radius.

Change of particle radius and particle porosity with time can be calculated as follows:

$$r_{P,\,t+\Delta t} = \sqrt[3]{r_{P,\,t}^3 - \frac{3\dot{m}_{C,S}}{4\pi\rho_P}\Delta t};\ \ \varepsilon_{P,t+\Delta t} = \varepsilon_{P,t} + \frac{\dot{m}_{C,V}\,\Delta t}{V_P\rho_C} \tag{4.21}$$

The volumetric-based and surface-based carbon mass flow can be calculated as follows [90]:

$$\dot{m}_{C,V} = V_P\ \left(\frac{M_C}{M_{CO_2}}\,\rho_{g,P}\,\underbrace{k\,S'''}_{k_{c,V}}\,Y_{CO_2,pp}\right), \tag{4.22}$$

$$\dot{m}_{C,S} = A_P\left(\frac{M_C}{M_{CO_2}}\,\rho_g\,k\,Y_{CO_2,pm}\right) \tag{4.23}$$

$k_{c,V} = k\,S'''$ is the volumetric kinetic rate constant with dimensions 1/s. Here $S''' = \frac{\sum S_{pores}}{Vol_p}$ is the internal specific surface area of the particle with dimensions 1/m. Total carbon consumption rate for one particle can be written as:

$$\dot{m}_P = \dot{m}_{C,V} + \dot{m}_{C,S} = A_P \, \frac{M_C}{M_{CO_2}} \, \rho_g \, k \, Y_{CO_2,pm} \left(1 + \frac{V_P}{A_p} S''' \, \frac{Y_{CO_2,pp}}{Y_{CO_2,pm}} \right) \tag{4.24}$$

After tracking the mass of the particle, heat and mass transfer equations for porous sample can be formulated as done earlier for non-porous particles with slight adjustments.

Energy conservation

Similar to the non-porous particle model, thermal energy balance inside the porous media takes the form:

$$V \left(\rho_g \, \varepsilon \, c_{p,g} \; + \; \rho_s \, (1 - \varepsilon) \, c_s \right) \frac{dT_{pm}}{dt} = \dot{Q}_{Wall} + \dot{Q}_{Gas} + \dot{Q}_{Reaction} \tag{4.25}$$

$$\dot{Q}_{Wall} = \lambda_{eff} \frac{A}{h/2} \left(T_w - T_{pm} \right) \tag{4.26}$$

$$\dot{Q}_{Reaction} = \left(\sum \left(\dot{m}_{C,V} + \dot{m}_{C,S} \right) \right) \Delta_R H = N_P \left(\dot{m}_P \right) \Delta_R H \tag{4.27}$$

Balance Interface-Char Layer

$$\dot{Q}_{Gas} = \lambda_{eff} \, \frac{A}{h/2} \, \left(T_S - T_{pm} \right) \tag{4.28}$$

Balance Ambient gas-Interface

$$\dot{Q}_{Gas} = \lambda_g \frac{A}{H - h} \left(T_\infty - T_S \right) + A \, \varepsilon_{emissivity} \, \sigma_{SB} \, \left(T_\infty^4 - T_S^4 \right) \tag{4.29}$$

CO_2 species balance for the gas phase inside the porous media

Species balance inside the porous media is now also effected by diffusion into the pores of the particles. Therefore, the species balance for CO_2 mass fraction takes the form:

$$\varepsilon \, V \, \rho_g \, \frac{dY_{CO_2,pm}}{dt} = \underbrace{(A\varepsilon) \, \frac{D_{eff}}{h} \, \rho_g \, \left(Y_{CO_2,S} - Y_{CO_2,pm} \right)}_{Diffusion \, from \, surface} - \underbrace{N_P \, \beta_{in} \, \rho_g \, \left(Y_{CO_2,pm} - Y_{CO_2,pp} \right)}_{Diffusion \, inside \, particles}$$

$$-\underbrace{k\,(\sum S_p)\,\rho_g\,Y_{CO_2,pm}}_{Surface\,Reaction}-\underbrace{N_P\,(\dot{m}_P)\,Y_{CO_2,pm}}_{Convection:\,Stefan\,Flow} \tag{4.30}$$

The internal mass transfer coefficient for diffusion inside the pores is calculated as follows:

$$\beta_{in} = 4\,\pi\,D_{\text{eff,P}}\left(\frac{1}{a_1\,r_P}-\frac{1}{r_P}\right)^{-1} \tag{4.31}$$

where $a_1 = 0.85$ represents the division of the particle in an outer shell and an inner particle with equal volume [93].

For pores within the particle, mean free path of gases is now comparable with that of pore radius and hence, we now also have to consider the Knudsen diffusivity for diffusion within the particles. The effective coefficient inside the porous particle is calculated from the two diffusion mechanisms: bulk diffusion and Knudsen diffusion.

$$D_{\text{eff,P}} = \frac{1}{\frac{1}{D_b}+\frac{1}{D_{kn}}} \tag{4.32}$$

The bulk diffusion coefficient can be estimated from the molecular diffusion and porosity of the particle.

$$D_b = {\varepsilon_P}^2\,(\varepsilon^2 D_g) \tag{4.33}$$

The Knudsen diffusion coefficient is calculated according to

$$D_{kn} = \frac{2}{3}\sqrt{\frac{8\,R\,T}{\pi\,M_i}}\,r_{pore} \tag{4.34}$$

where r_{pore} is the average pore radius.

Balance Ambient gas-Interface

Species balance at char surface is same as described previously for the non-porous particles.

$$(A\varepsilon)\,\frac{D_{eff}}{h}\,\rho_g\,(Y_{CO_2,S}-Y_{CO_2,pm}) = (A\varepsilon)\,\frac{D_g}{H-h}\,\rho_g\,(Y_{CO_2,\infty}-Y_{CO_2,S}) - N_p\,(\dot{m}_P)\,Y_{CO_2,S} \tag{4.35}$$

Mass transfer inside a single particle: CO_2 species balance

Internal species transport is affected by diffusion, heterogeneous reaction and stefan flow occuring inside the pores.

$$V_P\,\epsilon_P\,\rho_{g,P}\frac{dY_{CO_2,pp}}{dt} = \underbrace{\beta_{in}\,\rho_{g,P}\,\left(Y_{CO_2,pm}-Y_{CO_2,pp}\right)}_{\text{Diffusion}} - \underbrace{V_P\,S'''\,k\,\rho_{g,P}\,Y_{CO_2,pp}}_{\text{Heterog. chem.}}$$

$$- \underbrace{\dot{m}_{C,V}\,Y_{CO_2,pp}}_{\text{Stefan flow}} \tag{4.36}$$

Analogously, species balance equations for CO can be written as follows:

CO species balance for the gas phase inside the porous media

$$\varepsilon\,V\,\rho_g\,\frac{dY_{CO,pm}}{dt} = \underbrace{(A\varepsilon)\,\frac{D_{eff}}{h}\,\rho_g\,\left(Y_{CO,S}-Y_{CO,pm}\right)}_{Diffusion\,from\,surface} - \underbrace{N_P\,\beta_{in}\,\rho_g\,\left(Y_{CO,pm}-Y_{CO,pp}\right)}_{Diffusion\,inside\,particles}$$

$$+\underbrace{2\,\frac{M_{CO}}{M_{CO_2}}k\,(\sum S_p)\,\rho_g\,Y_{CO_2,pm}}_{Surface\,Reaction} - \underbrace{N_P\,(\dot{m}_P)\,Y_{CO,pm}}_{Convection:\,Stefan\,Flow} \tag{4.37}$$

Balance Ambient gas-Interface

$$(A\varepsilon)\,\frac{D_{eff}}{L_{ch}}\,\rho_g\,\left(Y_{CO,S}-Y_{CO,pm}\right) = (A\varepsilon)\,\frac{D_g}{H-h}\,\rho_g\,\left(Y_{CO,\infty}-Y_{CO,S}\right) - N_p\,(\dot{m}_P)\,Y_{CO,S} \tag{4.38}$$

Mass transfer inside a single particle: CO species balance

$$V_P\,\epsilon_P\,\rho_{g,P}\frac{dY_{CO,pp}}{dt} = \underbrace{\beta_{in}\,\rho_{g,P}\,\left(Y_{CO,pm}-Y_{CO,pp}\right)}_{\text{Diffusion}} + \underbrace{2\frac{M_{CO}}{M_{CO_2}}\,V_P\,S'''\,k\,\rho_{g,P}\,Y_{CO_2,pp}}_{\text{Heterog. chem.}}$$

$$- \underbrace{\dot{m}_{C,V}\,Y_{CO,pp}}_{\text{Stefan flow}} \tag{4.39}$$

Internal surface development

The consumption of carbon, alters the internal reactive surface area of the char particle. Different kinetic models accounting this change were discussed in section 1.3. In this work, the Random Pore Model developed by Bhatia and Perlmutter [46] is chosen to describe the evolution of the internal char structure as conversion proceeds. The expression for the same is as follows:

$$S''' = S_0'''(1 - X_C)\sqrt{1 - \psi\,(1 - X_C)} \tag{4.40}$$

Here ψ is a structural parameter of char and X_C is the char conversion with time. In this work, its value was chosen to be 4.0 [45].

4.4.1 Simplified model using Thiele Modulus

Another approach which is computationally easy to solve, can be applied to the porous particle model. The impact of pore diffusion can be evaluated using the well-known effectiveness factor η [74].

$$\eta = \frac{1}{\phi}\left(\frac{1}{\tanh(3\,\phi)} - \frac{1}{3\,\phi}\right) \tag{4.41}$$

where ϕ is the Thiele modulus and is defined as:

$$\phi^2 = \frac{k\,S'''\,r_p^2}{D_{eff}} \tag{4.42}$$

In this case, the CO_2 species concentration inside the particle can be estimated as

$$Y_{CO_2,pp} = \eta \cdot Y_{CO_2,pm} \tag{4.43}$$

Therefore, the total carbon consumption rate now becomes:

$$\dot{m}_P = A_P\,\frac{M_C}{M_{CO_2}}\,\rho_{g,S}\,k\,Y_{CO_2,pm} \cdot \left(1 + \frac{V_P}{A_p} S'''\eta\right) \tag{4.44}$$

In this case instead of two ODE for $Y_{CO_2,pp}$ and $Y_{CO_2,pm}$ we have only one ODE:

$$\varepsilon\,V\,\rho_g \frac{dY_{CO_2,pm}}{dt} = \underbrace{(A\varepsilon)\,\frac{D_{eff}}{L_{ch}}\,\rho_g\,(Y_{CO_2,S} - Y_{CO_2,pm})}_{Diffusion\,from\,surface} - \underbrace{(1-\varepsilon)V\,S'''\,k\,\rho_{g,P}\,\eta \cdot Y_{CO_2,pm}}_{\text{Heterog. chem.}}$$

$$\underbrace{-k\left(\sum S_p\right)\rho_g\, Y_{CO_2,pm}}_{Surface\,Reaction} \underbrace{-N_P\left(\dot{m}_{C,S}+\dot{m}_{C,V}\right)\, Y_{CO_2,pm}}_{Convection: Stefan\,Flow} \tag{4.45}$$

This approach is computationally more efficient than the 2-ODE approach. Steady state solutions of both the approaches were computed to confirm that they give similar results. Tables 4.2 and 4.3 display steady state results using both approaches for $S''' = 10^6$ and $Y_{CO_2,\infty} = 0.99$ at different inlet gas temperatures. As can be confirmed, both these models give almost similar results for a range of temperature.

Table 4.2: Steady state results from MatLab for $S''' = 10^6$ and $Y_{CO_2\infty}$=0.99 using 2 ODE approach

T_∞	T_P	$Y_{CO_2,PM}$	$Y_{CO_2,PP}$	$Y_{CO,PM}$	$Y_{CO,PP}$	$\dot{m}_{C,V}$	$\dot{m}_{C,S}$
800	799.833	0.9756	0.9756	0.0045	0.0045	6.557e-14	3.278e-16
900	895.677	0.6595	0.6595	0.1042	0.1042	1.8086e-12	9.044e-15
1000	985.952	0.147729	0.14753	0.2664	0.2665	6.207e-12	3.1078e-14
1100	1082.7	0.015014	0.014785	0.3087	0.3089	8.028e-12	4.0768e-14
1200	1182.7	0.001895	0.001663	0.3129	0.3130	8.42e-12	4.7987e-14

Table 4.3: Steady state results from MatLab for $S''' = 10^6$ and $Y_{CO_2\infty}$=0.99 using 1 ODE approach

T_∞	T_P	$Y_{CO_2,PM}$	$Y_{CO_2,PP}$	$Y_{CO,PM}$	$Y_{CO,PP}$	$\dot{m}_{C,V}$	$\dot{m}_{C,S}$
800	799.383	0.9779	0.9779	0.0045	0.0045	6.5812e-14	3.39e-16
900	895.49	0.68418	0.68418	0.1145	0.1145	1.886e-12	9.4307e-15
1000	985.656	0.153081	0.153081	0.3142	0.3142	6.38e-12	3.19e-14
1100	1082.7	0.014879	0.014879	0.3665	0.3665	8.0653e-12	4.032e-14
1200	1182.7	0.0017	0.0017	0.3714	0.3714	8.4362e-12	4.2181e-14

4.5 Solution methodology for the porous particle model

In this section, detailed methodology to solve unsteady equations using the simplified I ODE approach is presented. The system of equations representing the model was solved iteratively for each time step using MATLAB 2019 software. Flowchart of the algorithm used in MatLab is shown in Fig. 4.9 and the detailed methodology is described below it. Implicit iterative scheme was used to solve the equations which provided more flexibility and better stability for each time step.

After inputting the constants and updating the initial conditions, time loop is started and time after each iteration is calculated as:

$t(i+1) = i * dt$

Values from previous time step are used as initial guesses for implicit scheme.

Then internal iterations for that time step begin.

for j=1:100000

First properties like density of gas, heat capacity of gas, conductivity of gas in bulk gas and porous media are calculated. Diffusion coefficients for bulk gas and porous media are calculated using the fact that Lewis number is assumed to be unity. Kinetic rate constant is then calculated as:

$$k = A_0 \exp \frac{-E_A}{R\ T_{pm}(i+1)(j)}$$

Here (i+1) refers to the time step iteration and j refers to internal iteration.

Then, density of single particle is calculated according to Eq.4.18.

$$\rho_P = \rho_{g,P}\, \varepsilon_P(i+1)(j) + \left(1 - \varepsilon_P(i+1)(j)\right) \rho_C$$

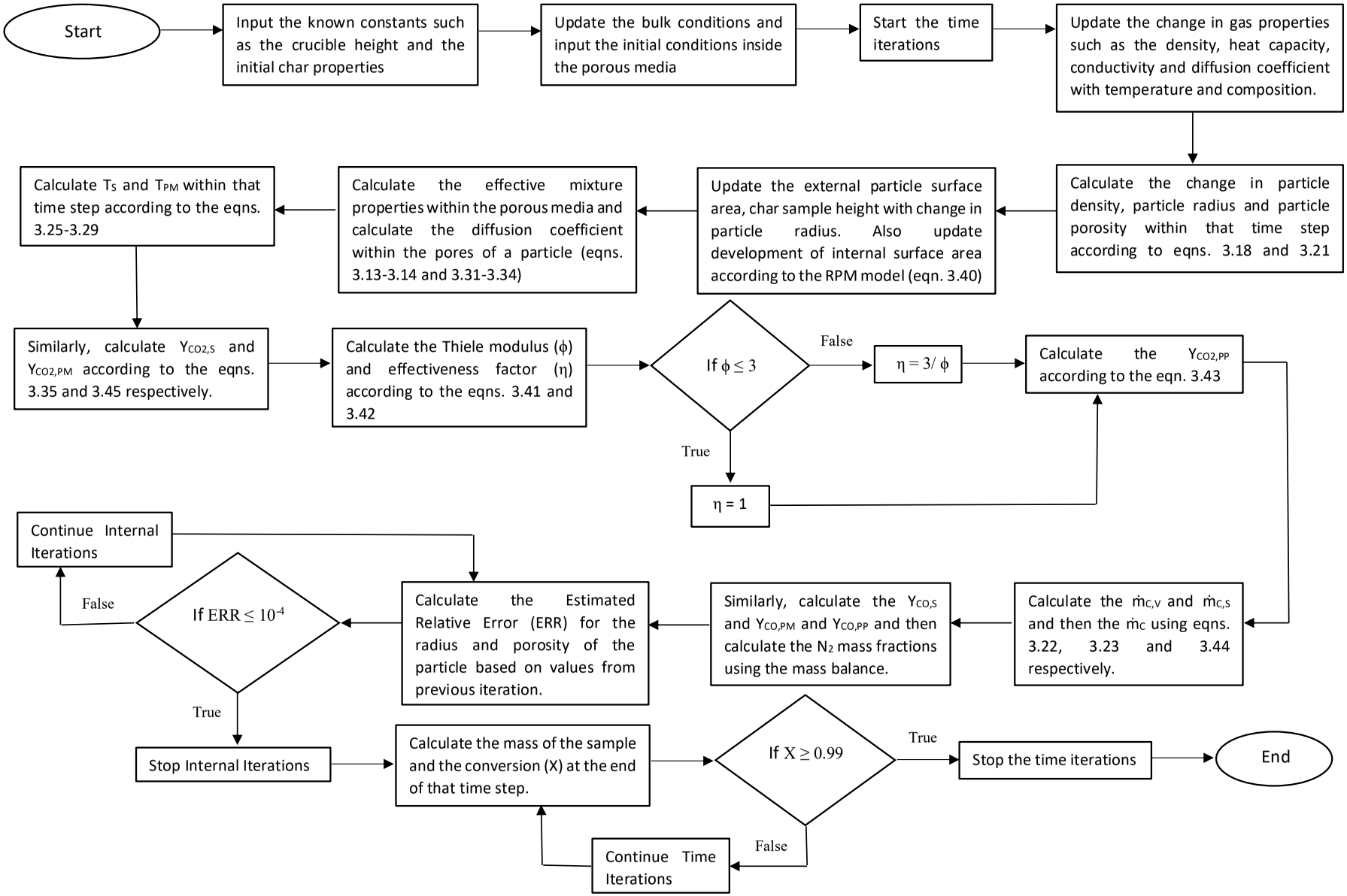

Figure 4.9: Fow chart of the MatLab algorithm

Then the change of particle radius and porosity with time is calculated in accordance with Eq. 4.21.

$$R_P(i+1)(j) = R_P(i) - \frac{\dot{m}_{C,S}(i+1)(j)}{4\,\pi\,R_P^2(i+1)(j)\,\rho_P}dt$$

$$\varepsilon_P(i+1)(j) = \varepsilon_P(i) + \frac{\dot{m}_{C,V}(i+1)(j)}{\frac{4}{3}\,\pi\,R_P^3(i+1)(j)\,\rho_C}dt$$

Change in particle radius causes the change in sample height. This can be calculated using the fact that number of particles in the sample (N_P) remain constant. Thus according to Eq 4.1 :

$$h(i+1)(j) = h(i) * \left(\frac{R_P(i+1)(j)}{R_P(i)}\right)^3$$

Accordingly, area of the particle (A_P), volume of the particle (V_P) and volume of the sample (V) are updated.

$$A_P(i+1)(j) = 4\,\pi\,R_p^2(i+1)(j)$$

$$V_p(i+1)(j) = \frac{4}{3}\,\pi\,R_p^3(i+1)(j)$$

$$V(i+1)(j) = A \cdot h(i+1)(j)$$

Change in internal surface area (S''') is calculated according to the RPM model as:

$$S''' = S_0\Big(1 - X(i+1)(j)\Big)\sqrt{1 - \psi\, ln\Big(1 - X(i+1)(j)\Big)}$$

where X is the conversion.

Next, effective porous media properties:porous sample conductivity (λ_{eff}), effective gas diffusivity within the sample (D_{eff}) and internal particle diffusion coefficient ($D_{eff,P}$)

are calculated using their respective formulas.

After updating particle radius, particle porosity and effective properties with time, equations depicting conservation of heat and mass transfer can now be solved.
First, the surface temperature (T_S) is calculated using Eqs. 4.28 and 4.29 employing Newton-Ralphson method.

$$T_S(i+1)(j) = T_S(i) - \left(\frac{1}{\frac{\lambda_eff}{h/2} + \frac{\lambda_g}{H-h} + 3\ \varepsilon_{emissivity}\ \sigma_{SB}\ T_S^3(i+1)(j)} \right) \left(\frac{\lambda_{eff}}{h/2}\ \Big(T_S(i+1)(j) - T_{pm}(i+1)(j) \Big) - \frac{\lambda_g}{H-h}\ \Big(T_\infty - T_S(i+1)(j) \Big) - \varepsilon_{emissivity}\ \sigma_{SB}\ \Big(T_\infty^4 - T_S^4(i+1)(j) \Big) \right)$$

Then, the particle temperature (T_P) is calculated using Eqs. 4.25-4.28.

$$T_{pm}(i+1)(j) = T_{pm}(i) + \left(\frac{dt}{V\big(\rho_g\ \varepsilon\ c_{p,g} + \rho_s\ (1-\varepsilon)\ c_s\big)} \right) \left(\lambda_{eff} \frac{A}{h/2} \Big(T_w - T_{pm}(i+1)(j) \Big) + \lambda_{eff} \frac{A}{h/2} \Big(T_S(i+1)(j) - T_{pm}(i+1)(j) \Big) + N_p\ \dot{m}_P(i+1)(j)\ \Delta_R H \right)$$

Next, the thiele modulus and the effectiveness factor are calculated.

$$\phi^2 = \frac{k\, S'''\, R_P^2(i+1)(j)}{D_{eff}}$$

Then effectiveness factor based on ϕ is calculated as
if $\phi < 3$, $\eta = 1$
else $\eta = 3/\phi$

Surface CO_2 mass fraction is calculated next according to Eq. 4.35.

$$Y_{CO_2,S}(i+1)(j) = \frac{(A\varepsilon)\ \frac{D_g}{H-h}\ \rho_g\, Y_{CO_2,\infty} + (A\varepsilon)\ \frac{D_eff}{h}\ \rho_g\, Y_{CO_2,pm}(i+1)(j)}{(A\varepsilon)\ \frac{D_g}{H-h}\ \rho_g\ +\ (A\varepsilon)\ \frac{D_eff}{h}\ \rho_g + N_P\, \dot{m}_P(i+1)(j)}$$

Next porous media CO_2 species mass fraction is calculated.

$$Y_{CO_2,pm}(i+1)(j) = Y_{CO_2,pm}(i) + \left(\frac{dt}{\varepsilon V \rho_g}\right)\Bigg((A\varepsilon)\frac{D_eff}{h}\rho_g\Big(Y_{CO_2,S}(i+1)(j) - Y_{CO_2,pm}(i+1)(j)\Big) \\ -(1-\varepsilon)\,V\,S'''\,k\,\rho_g\,\eta\,Y_{CO_2,pm}(i+1)(j) - k\,(\sum S_P)\,\rho_g\,Y_{CO_2,pm}(i+1)(j) \\ -N_P\;\dot{m}_P(i+1)(j)\;Y_{CO_2,pm}(i+1)(j)\Bigg)$$

Particle CO_2 mass fraction is then calculated using effectiveness factor.

$$Y_{CO_2,pp}(i+1)(j) = \eta\;\cdot Y_{CO_2,pm}(i+1)(j)$$

Next, $\dot{m}_{c,V}$ and $\dot{m}_{c,S}$ values are updated.

$$\dot{m}_{C,V}(i+1)(j) = V_P\left(\frac{M_C}{M_{CO_2}}\,\rho_g\,k\,S'''\,Y_{CO_2,pp}(i+1)(j)\right)$$

$$\dot{m}_{C,S}(i+1)(j) = A_P\left(\frac{M_C}{M_{CO_2}}\,\rho_g\,k\,Y_{CO_2,pm}(i+1)(j)\right)$$

$$\dot{m}_P(i+1)(j) = \dot{m}_{C,V}(i+1)(j) + \dot{m}_{C,S}(i+1)(j)$$

Similarly, CO species mass fractions are calculated .

$$Y_{CO,S}(i+1)(j) = \frac{(A\varepsilon)\,\frac{D_g}{H-h}\,\rho_g\,Y_{CO,\infty} + (A\varepsilon)\,\frac{D_eff}{h}\,\rho_g\,Y_{CO,PM}(i+1)(j)}{(A\varepsilon)\,\frac{D_g}{H-h}\,\rho_g + (A\varepsilon)\,\frac{D_eff}{h}\,\rho_g + N_P\,\dot{m}_P(i+1)(j)}$$

$$Y_{CO,pm}(i+1)(j) = Y_{CO,pm}(i) + \left(\frac{dt}{\varepsilon V \rho_g}\right)\Bigg((A\varepsilon)\,\frac{D_eff}{h}\,\rho_g\,\Big(Y_{CO,S}(i+1)(j) - Y_{CO,pm}(i+1)(j)\Big) \\ +2\,\frac{M_{CO}}{M_{CO_2}}\,(1-\varepsilon)\,V\,S'''\,K\,\rho_g\,\eta\,Y_{CO_2,pm}(i+1)(j) + 2\,\frac{M_{CO}}{M_{CO_2}}\,K\,(\sum S_P)\,\rho_g\,Y_{CO_2,pm}(i+1)(j) \\ -N_P\,\dot{m}_P(i+1)(j)\,Y_{CO,pm}(i+1)(j)\Bigg)$$

$$Y_{CO,PP}(i+1)(j) = \eta \cdot Y_{CO,PP}(i+1)(j)$$

Next, N_2 species mass fractions are calculated by mass balance.

$$Y_{N_2,S}(i+1)(j) = 1 - Y_{CO_2,S}(i+1)(j) - Y_{CO,S}(i+1)(j)$$

$$Y_{N_2,pm}(i+1)(j) = 1 - Y_{CO_2,pm}(i+1)(j) - Y_{CO,pm}(i+1)(j)$$

$$Y_{N_2,pp}(i+1)(j) = 1 - Y_{CO_2,pp}(i+1)(j) - Y_{CO,pp}(i+1)(j)$$

Estimated relative errors are then calculated based on the current iteration and previous iteration results.

$$ERR_1 = abs\left(\frac{R_P(i+1)(j) - tmp0}{R_P(i+1)(j)}\right)$$

where tmp0 is the $R_P(i+1)(j-1)$ value from the previous j iteration.

$$ERR_2 = abs\left(\frac{\varepsilon_P(i+1)(j) - tmp1}{\varepsilon_P(i+1)(j)}\right)$$

tmp1 is the $\varepsilon_P(i+1)(j-1)$ value from the previous j iteration.

If ERR_1 and $ERR_2 < 10^{-4}$, mass of the sample and conversion for that time step are calculated using the following equations.

$$M(i+1)(j) = M(i)(j) - N_P * \dot{m}_C * dt$$

$$X(i+1)(j) = 1 - \frac{M(i+1)(j)}{M_0}$$

Internal iterations are then stopped and, when conversion $(X) > 0.99$, time iterations are stopped. Results produced by the software are written into a data-sheet and then interpreted.

4.6 Evaluation of kinetic parameters: Experimental results and model implementation

4.6.1 Char characterization results

After segregation of the char particles between 190 and 205 μm, characterization tests of char were performed as discussed in chapter 2. The results from elemental analysis, proximate analysis, BET surface area tests, crucible dimensions and several other properties of char are summarized in Table 4.4 and Table 4.5 respectively. Weber et al. [94] has reviewed properties of different biochars including biochars from woody biomass and all the properties mentioned in these tables, fall in the ranges classified by the author.

Table 4.4: Ultimate and proximate analysis results of biochar

Ultimate Analysis (dry basis)	wt %
Carbon	89.59
Hydrogen	1.66
Nitrogen	0.36
Sulphur	0
Oxygen	8.39

Proximate Analysis	wt%
Moisture	0.73
Ash (dry)	5.84
Volatiles (dry)	11.29
Fixed Carbon (dry)	82.14

Table 4.5: BET surface area and other char properties

Property	Unit	Value
BET surface area	$m^2\,g^{-1}$	129.17
Char particle density	$kg\,m^{-3}$	1600
Particle diameter	μm	200
Void fraction	-	0.42
Initial Particle porosity	-	0.5
Crucible height	mm	3.3
Crucible diameter	mm	5.5
Initial Char height	mm	1.28

4.6.2 TGA gasification results

In order to gain kinetic data from experiments, retrieved experimental data of mass loss vs time was converted to conversion vs time for a specific gasification temperature. Conversion is calculated by:

$$X = \frac{M_{C,0} - M_C}{M_{C,0}} \tag{4.46}$$

where $M_{c,0}$ is the original sample carbon mass at the start of the experiment and M_c is the mass at a specific time. Fig. 4.10 and Fig. 4.11 display the conversion vs time and gasification rate vs conversion graphs respectively for different gasification temperatures. As expected, gasification rate increases as the process temperature increases. As the gasification temperature is increased 100 K from 1073 K to 1173 K, gasification rate increases more than fourfold and the time taken to reach 98% conversion reduces from 8900 s at 1073 K to 1600 s at 1173 K. The gasification rate reaches a maximum shortly after the gasification reaction starts for T=800 ^0C and T=850 ^0C. The preliminary reason for this has been proven to be associated with the fact that when gas is switched from inert to reactive, non uniform concentration of the reactive gas is responsible for this maximum gasification rate [36]. For 900 ^0C, the maximum rate is

observed at conversion around 0.5 which may be influenced by both gas dispersion and pore structure change. Following the maximum rate, for all three temperatures, there is a gradual decrease in the rate until 90% conversion is achieved. This is followed by a sharp decrease which is mainly due to the coalscence of micropores to form larger pores, leading to the loss of reactivity.

Now, the instantaneous char conversion rate as a function of conversion can be described using Random Pore Model (RPM) as follows:

$$\frac{-1}{M_{c,0}}\frac{dM}{dt} = \frac{dX}{dt} = K_{RPM}\,(1-X)\,\sqrt{1-\psi(1-X)} \tag{4.47}$$

Here, K_{RPM} is the intrinsic kinetic constant with dimensions s^{-1} and varies with temperature. ψ as discussed earlier is a structural parameter of char and in this work its value is taken as 4.0 [45]. Integrating Eq: 4.47 we can determine K_{RPM} from the experiments. Upon integration we get

$$K_{RPM} = \frac{2}{\psi}\,\frac{\sqrt{1-\psi\,\ln(1-X_2)} - \sqrt{1-\psi\,\ln(1-X_1)}}{t_2 - t_1} \tag{4.48}$$

Using Eq. 4.48, K_{RPM} can be determined for a particular gasification temperature. In this work, range of conversion from 0.1 to 0.9 was used to determine K_{RPM} as this ensured that build-up of quasi-stationary gas concentration at the start of experiments is excluded.

The kinetic parameters, A_0 and E_A can now be determined using Least Square Regression (LSR) of data between K_{RPM} and temperature according to Eq. 4.49

$$K_{RPM} = \frac{S'''}{\rho_{char}}\,M_C\,A_0\,\exp\frac{-E_A}{RT}\,C^n_{CO_2} \tag{4.49}$$

Here $C^n_{CO_2}$ is the concentration of CO_2 and n denotes the variation of K_RPM with respect to this concenctration. Since the TGA didn't facilitate the variation of concentration of the reactive gas, the value of n was assumed to be 1. The gained kinetic data from the experiments is represented in Table 4.6.

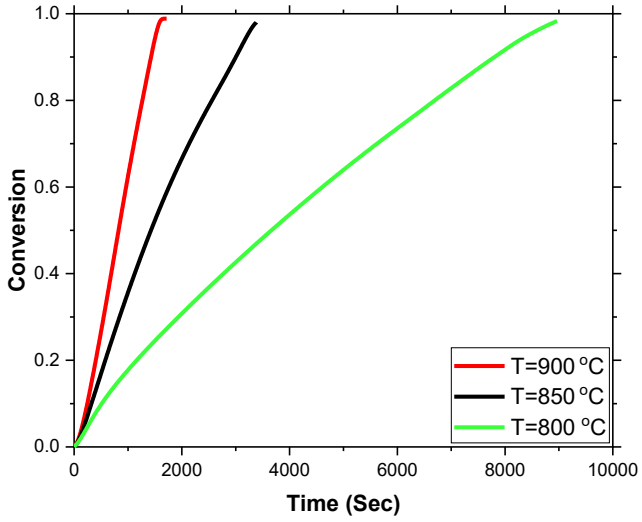

Figure 4.10: Experimental carbon conversion depending on time for different temperatures

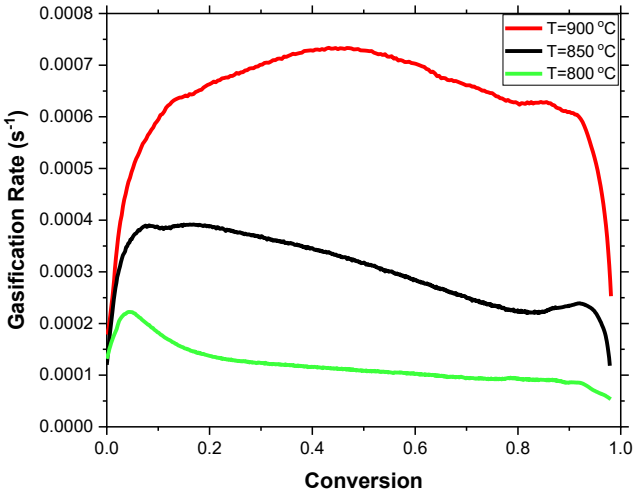

Figure 4.11: Gasification rate of the char at different gasification temperatures

Table 4.6: Kinetic parameters derived from the experimental data and model-based conditions

Kinetic parameter	Unit	Experimental	Model-based
A_0	$m\,s^{-1}$	$1.20 \cdot 10^2$	$4.138 \cdot 10^2$
E_A	$kJ\,mol^{-1}$	190.528	206.731

4.6.3 Model implementation to gain re-evaluated parameters

To implement the proposed model and take into account the effects of diffusional resistance within the crucible and within the pores, the experimentally determined kinetic parameters are used as initial input for the proposed model. Bisection method was then used to re-evaluate new parameters such that the the relative error of the weighted average $Y_{CO_2,pm}$ within the crucible was less than $< 10^{-4}$ and the curves predicted by the model were in conjunction with the experimental curves. The conversion curves for the biochar gasification as determined experimentally and as predicted by the model using model-based kinetic parameters are shown in Fig. 4.12 and the model-based kinetic parameters are represented in Table 4.6. As seen in Fig. 4.12, conversion vs time curves predicted by the model for the new set of determined kinetic parameters are in good agreement with the experimental curves. Difference between the experimental and the model-based values of these parameters show, how important it is to take into account the diffusion within the voids and within the crucible while determining the intrinsic reaction rate.

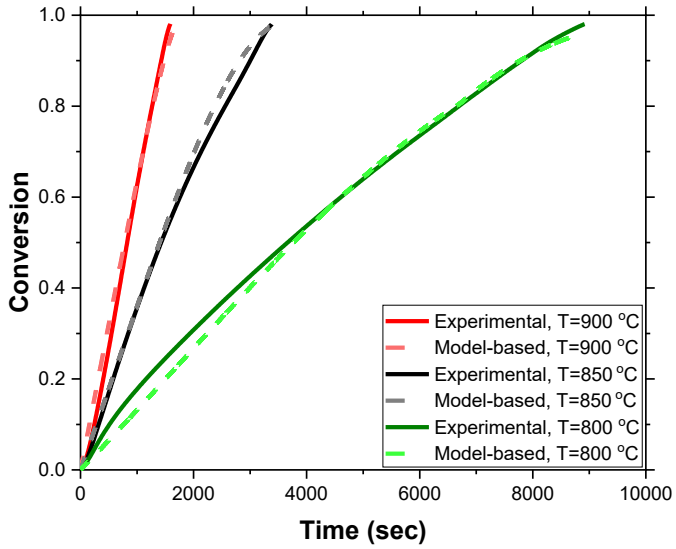

Figure 4.12: Conversion vs time curves for the char gasification as determined experimentally and as predicted by the proposed model

Fig. 4.13 compares the model-based and experimentally determined gasification rate vs conversion curves at different gasification temperatures. The curves are compared between conversion points 0.1 and 0.9 to take out the influence of dispersion of reactive gas during the start of the reaction. For all three temperatures the model predicts a gradually decreasing reactivity as the conversion increases. This is in line with the experimental results for temperature $850\,^0C$ and $800\,^0C$ as seen in the figure. For the temperature $900\,^0C$ there is some discrepancy between the experimental curve and the data predicted by the model, because the maximum rate at that temperature is observed around $\mathrm{X} = 0.5$ and there after it starts gradually decreasing.

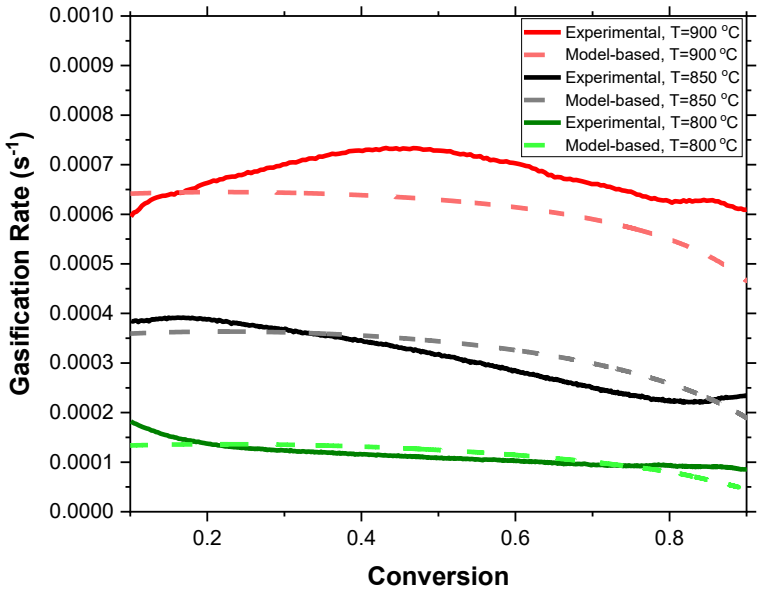

Figure 4.13: Gasification rate vs conversion curves for the char gasification as determined experimentally and as predicted by the proposed model

4.7 Sensitivity analysis

Re-evaluated kinetic parameters using the 0-D model were calculated in the previous section. It makes an interesting study to tweak some char properties and see how the reactivity responds to these changes. Thus, in this section a sensitivity analysis of the model is performed to see how the results at $\mathrm{T} = 900\,^{0}C$ vary with these changes. For all the parameter tweaks, A_0 and E_A determined in the previous section were used. Model sensitivity was analysed for the following three changes corresponding to the char properties:

1) Changing the tortuosity (τ) of voids within the sample and within the pores of the particle to 1.

2) Changing the specific surface area (S''') value of the sample to 10^7.

3) Changing the char structural parameter (ψ) value to 1 and 15.

The results and findings from these changes are discussed one by one.

4.7.1 Changing the tortuosity (τ) of voids within the sample and within the pores of the particle to 1

To evaluate the kinetic parameters using the 0-D model, tortousity of the curves within the void spaces between the particles and inside the pores of the particles had been lumped into $\frac{1}{\varepsilon}$. To assess the sensitvity analysis of the model with respect to tortousity, another case considering $\tau = 1$ was solved in MATLAB. For this case Eq. 4.14 and Eq. 4.33 change to $D_{eff} = \varepsilon\, D_g$ and $D_b = \varepsilon_P\, (\varepsilon D_g)$ respectively. To gauge the effect of this change, the model was run using the kinetic parameters determined in Table 4.6 in the previous section. The conversion vs time and gasification rate graphs for $T_\infty = 900\,^0C$, comparing the experimental data and the model-based results for two corresponding cases of τ are shown in fig. 4.14 and fig. 4.15. As can be seen from the figure, upon decreasing the tortuosity value to 1 prediction from the model deviates from the experimental results significantly. The gasification rate increases and the conversion occurs more rapidly.

This increase in the gasification rate predicted by the model is in line with the expected variation, because the value of tortuosity equal to 1 signifies that the void passages between the particles are essentially straight lines making it easier for the bulk gas to diffuse between them, hence increasing the gasification rate.

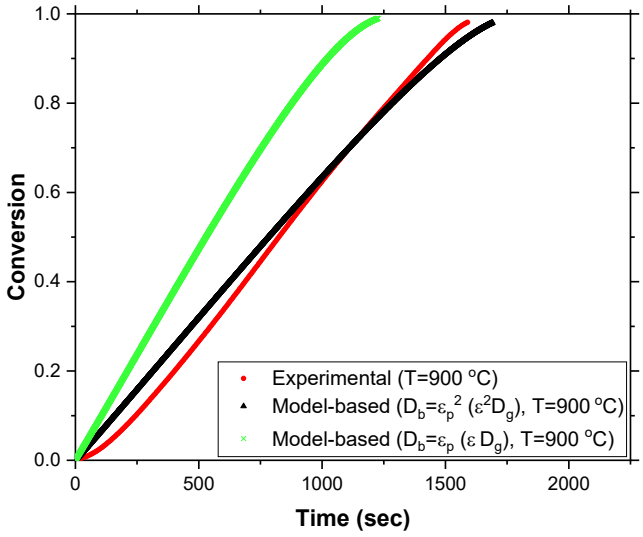

Figure 4.14: Conversion of char sample with time for $T_{bulk} = 900\,^0C$ as determined experimentally and as predicted by model for τ=$\frac{1}{\varepsilon}$ and $\tau = 1$

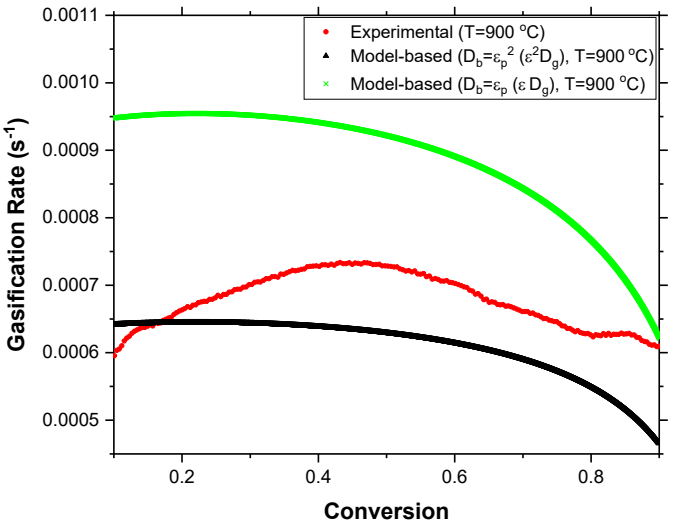

Figure 4.15: Gasification rate of the char sample with conversion for $T_{bulk} = 900\,^0C$ as determined experimentally and as predicted by model for τ=$\frac{1}{\varepsilon}$ and $\tau = 1$

4.7.2 Changing the specific surface area (S''') of the sample to 10^7

Specific surface area (SSA) of the char was measured using the BET experiments. Its volumetric value for the biochar was measured as $2.06 \cdot 10^8\, m^{-1}$. Another case of sensitivity analysis of the model was performed by changing the specific surface area (S''') and studying its impact on the reactivity of char. To study the effects of this change, the value of S''' was changed to $10^7\, m^{-1}$ keeping the kinetics same and its results were compared with original results. Figures 4.16 and 4.17 display this comparison at $\mathrm{T} = 900\,^0C$. Decrease in S''' considerably decreases the gasification rate and it takes almost triple the time to reach full conversion. Again the model correctly predicts the effects of SSA change on reactivity, as higher the SSA available, higher the concentration of the active sites for the reaction to take place, hence higher the reactivity.

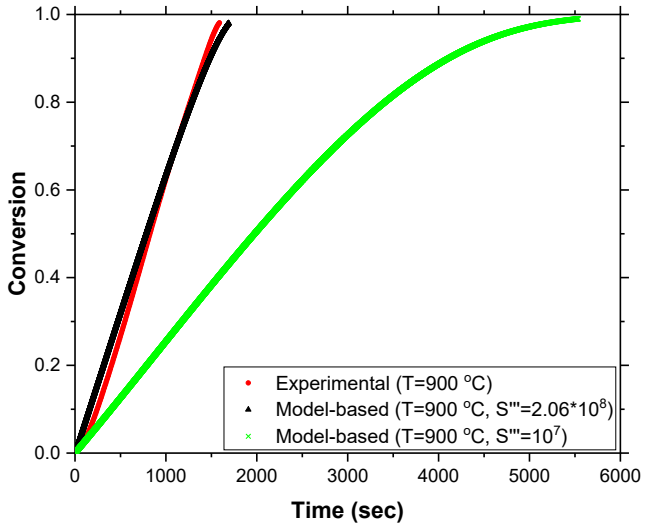

Figure 4.16: Conversion of char sample with time for $T_{bulk} = 900\,^0C$ as determined experimentally and as predicted by model for $S''' = 1.29 \cdot 10^8\, and\, S''' = 10^7$

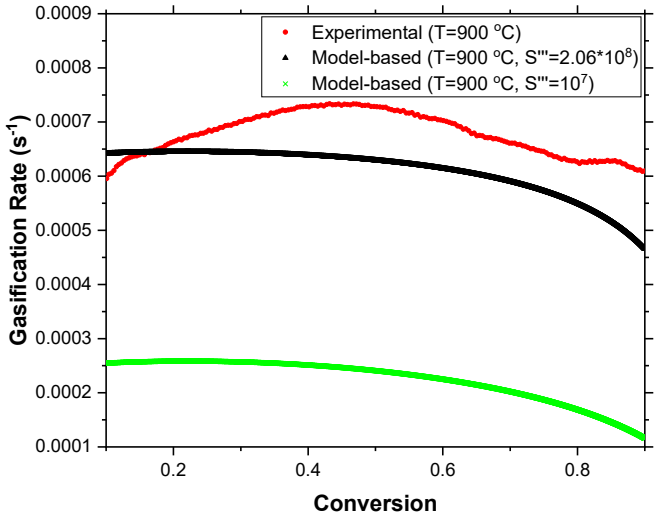

Figure 4.17: Gasification rate of the sample with time for $T_{bulk} = 900\,^0C$ as determined experimentally and as predicted by model for $S''' = 1.29 \cdot 10^8\, and\, S''' = 10^7$

4.7.3 Changing the char structural parameter (ψ) value to 1 and 15

Structural parameter of char (ψ) in the RPM function predicts the evolution of pore structure during the gasification. A high ψ value means that initially, the particle has a very little porosity and as the reaction proceeds, porosity increases with more and more reactions occuring within the pores, thus increasing reactivity [45]. Similarly, a low value of ψ relates to high initial porosity within the particle. This means that the particle is mostly consisted of macro and meso-pores and fewer micro-pores which are mostly responsible for the reaction rate within the pores. As a result, the gasification rate is slower because there's not much further development in the porous structure of the char [95]. This observation is comfirmed by the model in figures 4.18 and 4.19. As the ψ value is increased from 1 go 15, the gasification rate increases and the conversion of char happens faster.

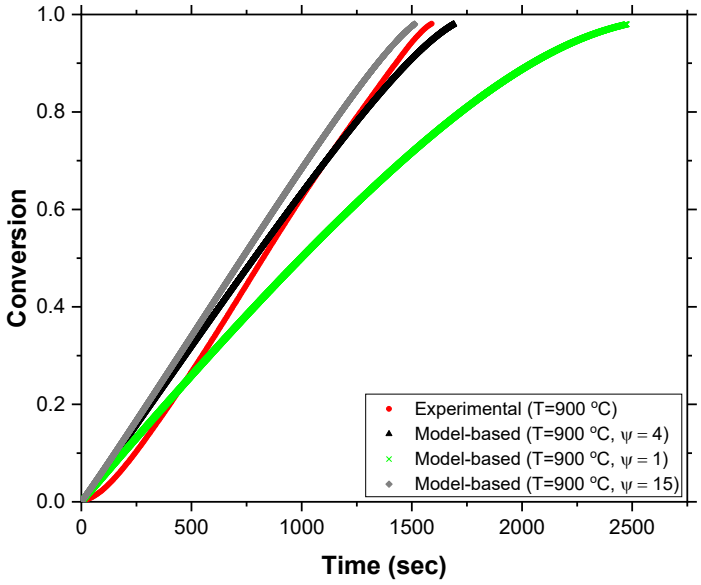

Figure 4.18: Conversion of char sample with time for $T_{bulk} = 900\,^0C$ as determined experimentally and as predicted by model for $\psi = 1$, $\psi = 4$ and $\psi = 15$

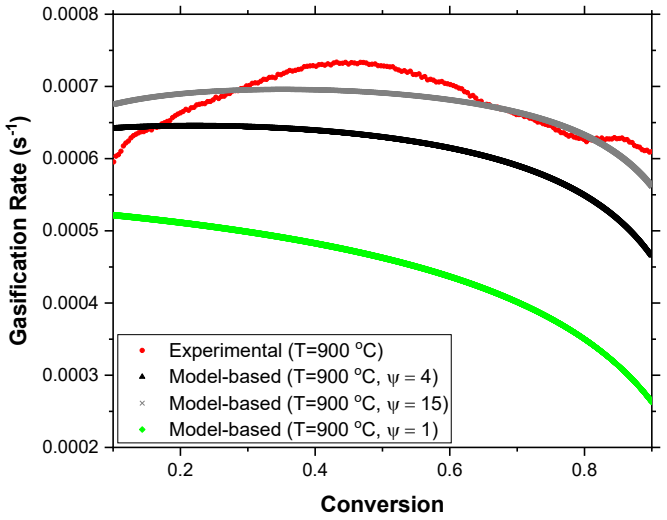

Figure 4.19: Gasification Rate of the sample with time for $T_{bulk} = 900\,^0C$ as determined experimentally and as predicted by model for $\psi = 1$, $\psi = 4$ and $\psi = 15$

4.8 Conclusion

This chapter presented a novel model to calculate intrinsic kinetics of char gasificationo using a TGA. The model followed a 0-dimensional approach and heat and mass transfer phenomenons within the crucible were expressed in terms of numerical transport equations. First, the equations were written for non porous char particles and validated against 3-D CFD simulations of the gasifying char particles published in [75]. Figures 4.4-4.7 compare the results from steady state solution of the model and data from CFD simulations. The correspondence between both the data sets was convincing with slight deviations at higher temperatures and the model was validated.

Next, the model was extended to porous particles, to take into account change in particle radius and particle porosity as the reaction proceeds. This was done by tracking the mass of each particle with time. Mass and heat transfer equations were updated to take into context pore diffusion and reaction inside pores. Another approach to deal with pore diffusion was applied using the thiele modulus and effectiveness factor. This approach ensured that only one ODE for species transport was required to be solved thus making the computations easy for software to process. In the next section, a detailed solution methodology that was used to solve the unsteady state equations was explained.

Experimental TGA results were then discussed and kinetic parameters were obtained from these results using the RPM model. Then the model was implemented to gain re-evaluated parameters. Obtained parameters using RPM were first inputted into the model and then these were tuned using the bisection model. Figures 4.12 and 4.13 confirm that the model reproduced similar results as compared to the experiments using the newly obtained parameters. In the last section, a sensitivity analysis of the model was performed by changing char properties and observing the behaviour of gasification rate with these changes. In this section also, the model showed good applicability as the behaviour of reactivity predicted by the model was similar to what has been observed in numerous experimental studies before hand.

Chapter 5

Evaluation of synergistic effects between biomass and plastics: Results and Discussion

5.1 Feed characterization

Elemental and Proximate analysis of the SW and HDPE were performed using the procedures discussed in 2.1.2. The results are displayed in Table 5.1. As can be seen, biomass contains carbon and oxygen in almost equal amounts, therefore highlighting the problem of high oxygen content in its bio-oil. On the other hand, HDPE evidently has no oxygen content, making it a ideal co-feedstock for pyrolysis. As can been seen from the results, HDPE contains all its organic matter in volatile form and does not contribute in forming char.

Table 5.1: Ultimate and Proximate analysis results of SW and HDPE feedstock

Ultimate Analysis (dry basis wt%)	SW	HDPE
Carbon	48.16	85.42
Hydrogen	5.90	14.39
Nitrogen	< 0.2	0
Sulphur	0	0
Oxygen	45.74	0
Proximate Analysis (wt%)		
Moisture	3.46	0
Ash(dry)	2.15	0
Volatiles (dry)	77.20	100
Fixed carbon	16.19	0

5.2 Pyrolysis characteristics of the samples

Pyrolysis of pure samples and their different blends was performed in the TGA. Weight loss curves and the respective DTG curves obtained from pyrolysis of samples are presented in Fig. 5.1 and Fig. 5.2 respectively. Softwood decomposition started at around $210\,^0C$ and was characterized by mainly two stages. In the first stage which lasted until $420\,^0C$, the biomass lost about 65% of its weight in a single stage. This corresponds to the degradation of cellulose and hemicellulose which comprise about 60-70% of the biomass's weight. In the second stage, slow decomposition of biomass's lignin content took place above the temperature $420\,^0C$ in a broad range. These results were consistent with the data in published literature regarding individual pyrolysis of biomass contents [12]. HDPE which consisited of 100% volatiles, decomposed in a short single stage as expected. The temeprature range for its decomposition ranged from $380 - 510\,^0C$. The maximum DTG peaks for pure samples corresponding to their weight loss curves were observed at T=$375\,^0C$ (17.86 %/min) for softwood and at T=$490\,^0C$ (51.85 %/min) for

HDPE respectively.

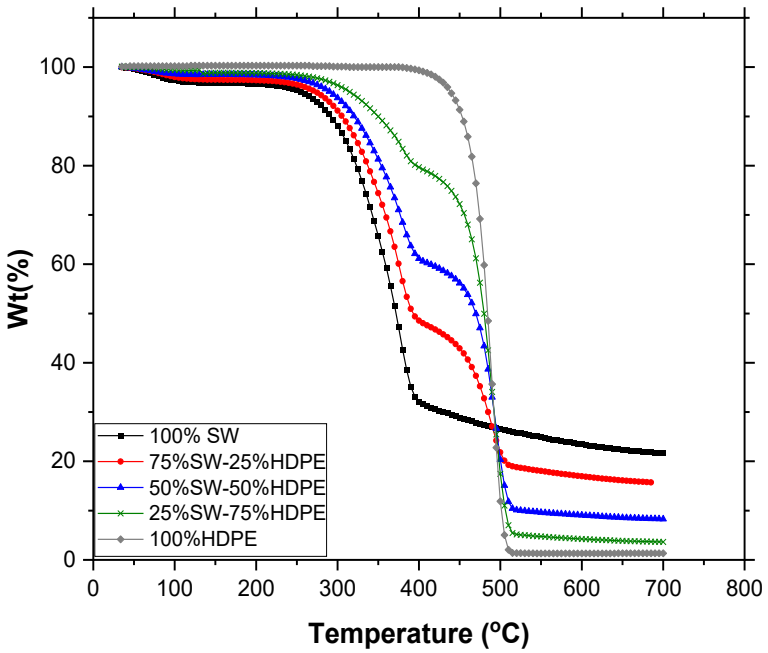

Figure 5.1: Weight percent vs temperature curves of pyrolysis of pure samples and their different blends in a TGA

The TG and DTG curves for the blends of SW and HDPE are also presented in Fig. 5.1 and Fig. 5.2. The TG and DTG curves of all the blends lie in between the SW and HDPE curves and the final residue was corresponding to their blending ratio. The decomposition took place in two stages for all the mixture samples. The first stage was due to the degradation of biomass and the second stage corresponded to the HDPE decomposition. As can be seen, with the increase of HDPE in the mixture, the maximum DTG peak regarding cellulose decomposition decreased thus signifying the effect of plastic coating reported in literature [77]. Also the starting decomposition temperature of the blends was delayed by $20\,^0C$ for the composition of 75%SW-25%HDPE and this delay increased to about $40\,^0C$ for the blending ratio of 25:75 and the temperature

for first peak regarding the cellulose degradation also increased with the blending ratio of HDPE. Also the termination temperature relating to pyrolysis state from HDPE was reduced for blends as compared with the pure sample, indicating that the releasing of volatiles was facilitated [81].

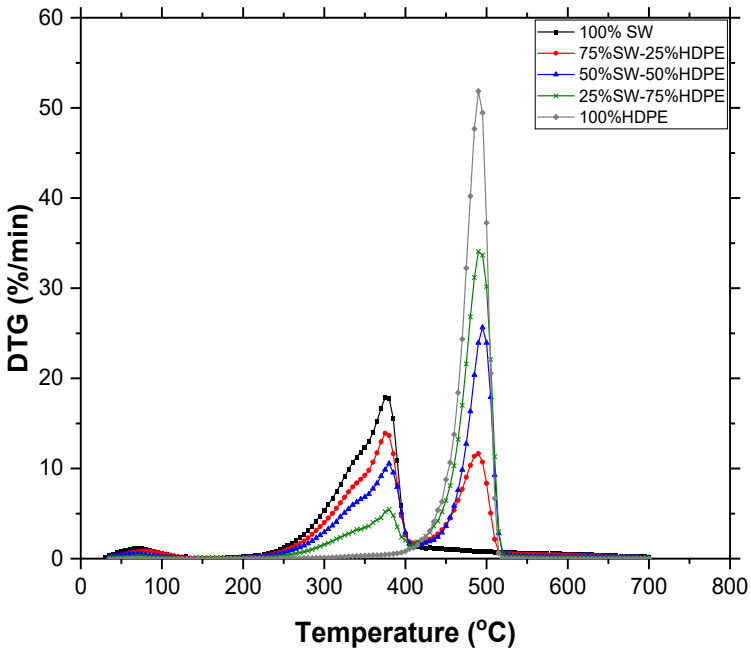

Figure 5.2: DTG curves of pyrolysis of pure samples and their different blends in a TGA

5.3 Synergistic effects between the SW and HDPE

In order to evaluate the the synergistic effects and get a better understanding of these effects, theoretical weight loss curves of the blends were calculated using the ratio of the pure samples and their individual curves. This approach has been readily applied in the literature by different authors while studying the synergistic effects [79]. The idea behind this approach is that if no synergistic interactions take place between the biomass and plastics, then the weight loss predicted by the theoretical curves should

be similar to the one determined experimentally. The theoretical weight loss curve is calculated using the following equation [79]:

$$W_{theoretical} = x_{SW} W_{SW} + x_{HDPE} W_{HDPE} \tag{5.1}$$

where x_{SW} and x_{HDPE} are the blending ratios of the softwood and HDPE respectively and W_{SW} and W_{HDPE} represent the values of weight loss during the pyrolysis of softwood and HDPE at same conditions as that of blends. Therefore, this should be the weight loss if it is assumed that the pyrolysis of SW and HDPE in a mixture are independent of each other. Based on this fact, the synergistic effects can be quantified by studying the discrepancy between the $W_{experimental}$ and $W_{theoretical}$ curves. The difference between the two quantities is described as follows:

$$\Delta W = W_{experimental} - W_{theoretical} \tag{5.2}$$

Fig. 5.3 shows the ΔW curves for blends of the SW and HDPE. Significant deviations can be seen for the temperature range where SW and HDPE degrade, thus confirming the synergistic interactions between the two compounds. Upto temperatures around $300\,^0C$, the deviation of ΔW was within the $\pm 1\%$, suggesting that no interactions had taken place because HDPE hadn't started decomposing. For the blending ratios of 50:50 and 25:75, there was a decrease in ΔW uptil $440\,^0C$ followed by a sharp rise at around $500\,^0C$ after which it remained constant for the rest of the temperature range.

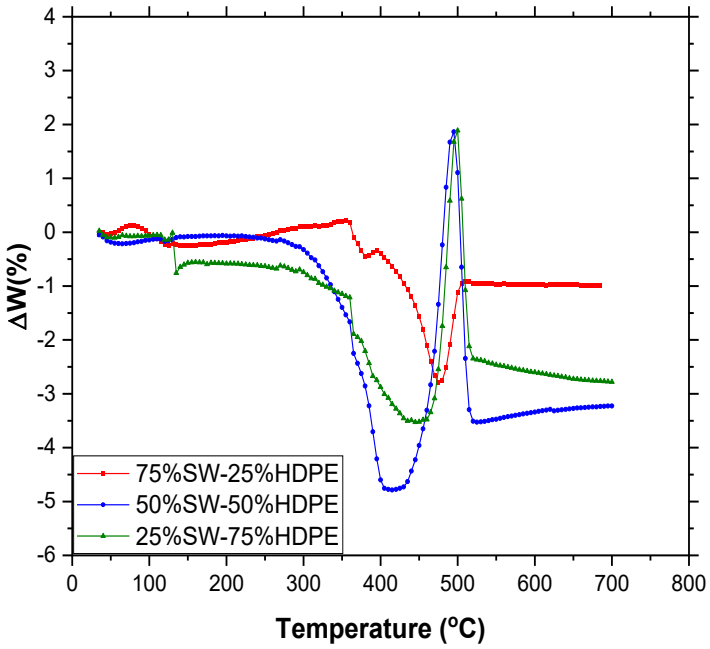

Figure 5.3: ΔW curves for blends of SW and HDPE

Other researchers have also reported similar behaviour between the biomass and plastic ΔW curves ([77], [82]). This behaviour can be attributed to the mechanism discussed in 1.6.2. HDPE first softens at around $300\,^0C$ reaching a plastic state and coats the biomass particles. This coating then inhibits the release of volatiles from SW decomposition and thus ΔW decreases. The second peak in the curves was achieved when plastic began to decompose and there was a large release of volatiles. This peak coincides with the DTG peak corresponding to the HDPE decomposition. Therefore ΔW increased. The positive value of ΔW confirmed the fact that biomass radicals abstracted hydrogen from the plastic and facilitated its decomposition in turn releasing more volatiles along with stabilizing the primary products from biomass decomposition and reducing char yield [81]. For the blending ratio of 75:25 however, only one negative peak was observed at around $460\,^0C$ and the final value was close to 0. A possible reason for this unusual characteristic can be the fact that the duration of HDPE softening

process extended and this resulted in negative value of ΔW between temperatures $400 - 520\,^0C$. A similar phenomenon was reported by Xiong et al. [77].

5.4 Char yield using tube furnace

In order to gasify the chars formed using blends, tube furnace was used to produce chars. Experimental details were provided in section 2.2.3. It has been discussed that synergistic effects between biomass and plastics tend to produce less char and favour the release of volatiles. This can also be verified from Fig 5.3, where the final ΔW values are below 0, thus confirming that less char is produced experimentally then predicted by theoretical formulation. This trend was also observed in tube furnace experiments.

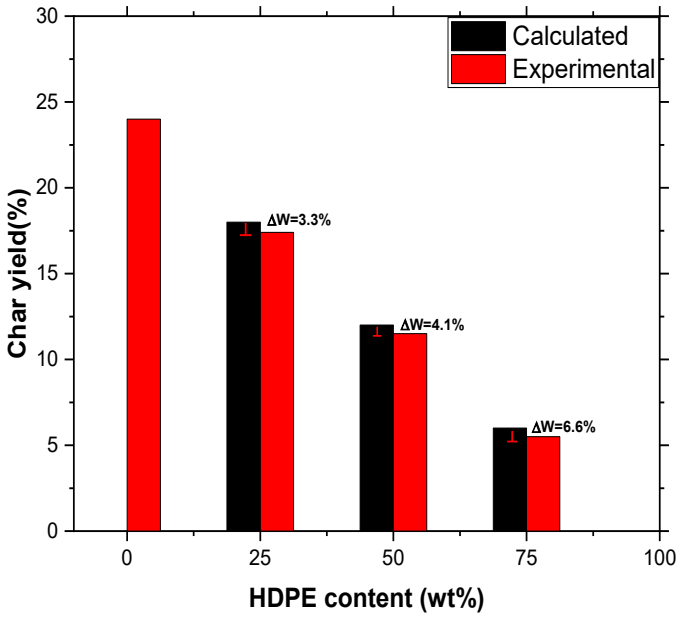

Figure 5.4: Char yield of blends obtained experimentally using tube furnace compared with calculated yield in case of no interactions

Fig. 5.4 displays comparison between experimentally obtained char yield of different blends using a tube furnace in comparison with theoretically calculated yields, that

would have been possible if no interaction took place. It can been seen char yield decreases as much as 6.6% for the case blending ratio of 25:75, thus confirming the fact that HDPE radicals stabilize primary products from cellulose decomposition of SW by donating hydrogen and later the radicals from HDPE catalyze lignin decomposition, releasing more volatiles and reducing the char formation.

5.5 Char characterization

Elemental analysis, BET surface area and SEM analysis of the char were performed to study its properties and characterize them on the basis of these observations. The results are discussed below.

5.5.1 Elemental analysis

The elemental analysis results of the chars formed are displayed in Table 5.2. It can be seen that as the blending ratio of HDPE increases, carbon content in the char increases significantly and as a result, the oxygen content within the chars formed also decreased. The hydrogen content of the char derived from blends also decrease when compared with the char derived directly from pure SW. The increase in fixed carbon content and the likewise decrease in hydrogen and oxygen contents of the chars point towards the fact that more hydrogen and oxygen containing groups were released during the pyrolysis of SW with blends of HDPE and thus confirming the fact that synergistic effects between biomass and plastics garvitate towards the release of more volatiles [94].

Table 5.2: Elemental analysis of chars fderived from pyrolysis of blends using SW and HDPE

Ultimate Analysis (dry basis wt%)	100% SW char	75%SW-25%HDPE char	50%SW-50%HDPE char	25%SW-75%HDPE char
Carbon	81.92	85.93	86.72	87.14
Hydrogen	3.17	2.84	2.8	2.9
Nitrogen	< 0.2	< 0.2	< 0.2	< 0.2
Sulphur	0	0	0	0
Oxygen	14.9	11.23	10.48	9.96

The H/C and O/C atomic ratios of the chars are presented in Fig. 5.5. It can be discerned from the figure that the H/C ratio of the char decreases 14.65 % (from 0.464 to 0.396) as the SW is blended with 25% HDPE. The O/C ratio also decreases 27.94% when SW is blended with 25% HDPE. On further increasing the HDPE weight percent, such a drastic impact on the atomic ratios ratios was not observed but still some effect are present. The O/C ratio continues to decrease as the blending ratio increases and H/C decreases for 50-50 wt% ratio but increases slightly for 25-75 wt% ratio probably due to inconsistency of the char particles used for analysis. A low H/C ratio is a indication that char predominately consists of fixed carbon aromatic rings, thus making it chemically more stable and improves its reactivity by increasing the active carbon sites [38].

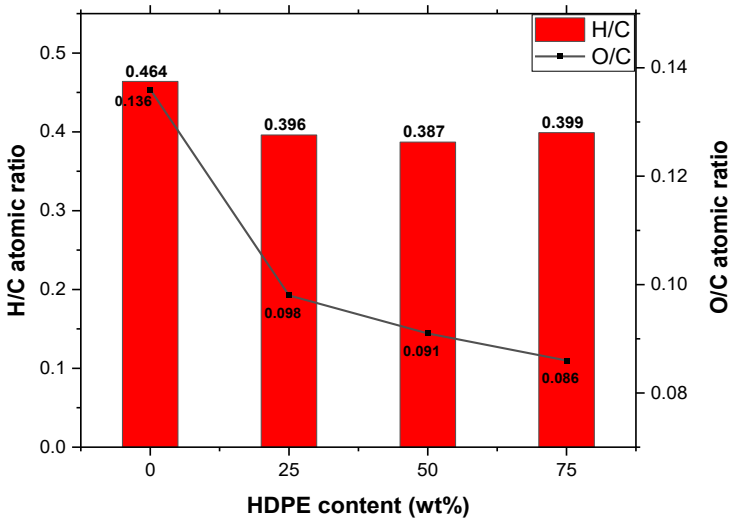

Figure 5.5: H/C and O/C atomic ratios of the chars derived pyrolysis of blends using SW and HDPE

5.5.2 SEM and BET analysis of the chars

The SEM images of the raw SW and the chars derived from pyrolysis of blends of SW and HDPE are presented in Fig. 5.6. As can be seen from images, raw SW particles (image a) had an amorphous, lumpy dense mixture having a compact structure with minute pores and mostly closed channels. This is also evident from the BET results of the samples presented in Table 5.3 where the surface area of raw SW was a negligible 0.164 m^2/g thus reproducing the fact that the raw biomass has an undeveloped pore structure. Upon thermal cracking of the SW, structure morphology of the char (image b) changed completely as compared with the raw SW particles. The char formed contained a fibrous and more fragmented structure with open pores formed due to the release of volatiles. This led to a large increase in the surface area of the char when compared to raw SW. The BET surface area value of 100% SW char was 85 m^2/g. The char morphology images of the blends of SW and HDPE are presented in images c, d and e respectively. The images show that the with the blending of HDPE, more

ruptures within the fragmented structure were caused upon pyrolysis, thus suggesting that more volatiles were released upon blending of HDPE leading to a more porous and less denser char. This was also evident from the BET surface area results. The surface area of blends increased from 85 m^2/g for 0 wt% of HDPE to 109 m^2/g for 75 wt% of HDPE within the sample.

Table 5.3: BET surface areas of Raw SW and chars derived from blends of SW and HDPE

Sample name	BET surface area (m^2/g)
Raw SW	0.164
100% SW char	88.45
75% SW-25% HDPE char	93.37
50% SW-50% HDPE char	101.14
25% SW-75% HDPE char	109.20

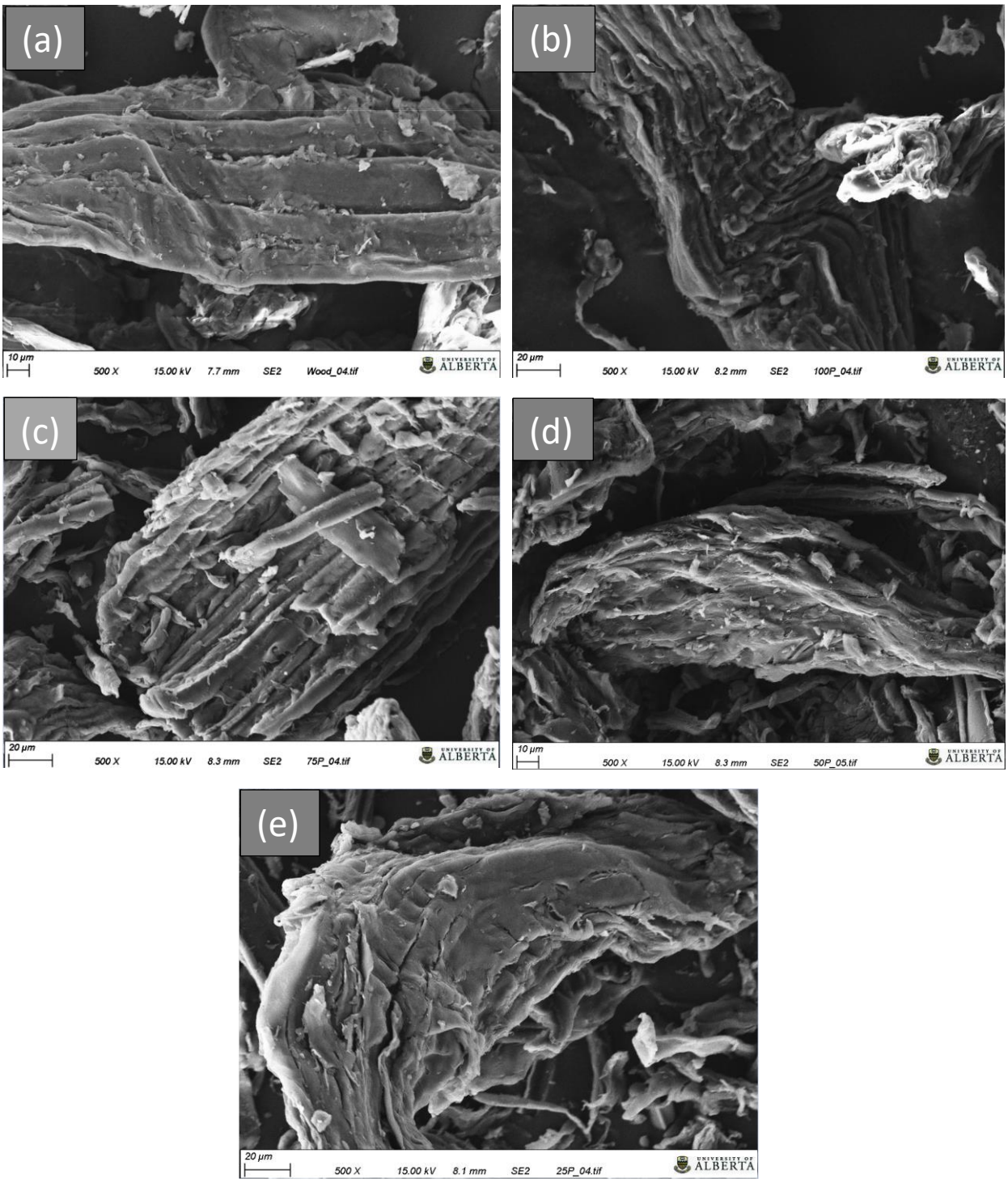

Figure 5.6: SEM images of (a) raw SW, (b) 100% SW char, (c) 75% SW-25% HDPE char, (d) 50% SW-50% HDPE char, (e) 25% SW-75% HDPE char

5.6 Gasification reactivity of chars

Char characterization techniques implied in the previous section provided valuable information regarding how the chars formed using different blending ratio of plastics are different from char from biomass alone. High carbon content, low O/C ratio, increased BET surface area suggest that the char formed using blends of plastics and biomass has improved properties due to release of more volatiles and thus might be more suitable for gasification processes. Co-gasification of biomass and plastics have reported to have synergistic effects in terms of increase in yield of total syngas produced and individual components such as H_2 and CO [88]. Therefore, the reactivity of chars during CO_2 gasification is discussed in this section.

The methodology of the experiments performed is discussed in chapter 2. Since the char formed from tube furnace experiments using blending ratio of 25-75 was low in quantity, it was not used for experiments. Rest all three chars were gasified in CO_2 atmosphere at three different temperatures i.e $800\,^0C$, $850\,^0C$, $900\,^0C$. Different chars had different volatile content present within them, which was released during the inert conditions maintained initially within the TGA, to increase the temperature from room temperature to the desired gasification temperature. As a result, by the time gasification reactions started, different samples had different weights. Therefore to normalize the weight and compare reactivities of the samples, data for the first 3.5 mg of weight loss of each sample from the time the gas was switched from inert N_2 to CO_2 was used to compare and characterize the gasification rates. The conversion vs time graphs of the three chars gasified at different temperatures are presented in Fig. 5.7. It can be seen that the time required to achieve 3.5 mg weight loss for the chars formed using blends (blue and green scatter) is significantly less than the char formed from 100% biomass (red scatter), for all three temperatures. This can attributed to the fact that during characterization, chars formed using blends had a higher carbon content and a larger BET surface area as compared with char formed from 100% biomass. Thus more active sites were present in the chars formed using blends which promoted re-

activity and hence the time required to achieve the desired conversion was reduced. Upon increasing the blending ratio to 50-50 wt%, further improvement in reactivity was observed for tmeperatures $850\,^0C$ and $900\,^0C$, however this was not congruent with the graphs obsevred at T=$800\,^0C$. The change observed was significant upon increasing the blending ratio as the carbon content in both the chars was similar as can be seen in Table 5.2. Thus, it can be concluded that synergistic effects between SW and HDPE observed during their co-pyrolysis not only improved its properties in terms of its elemenal content, increased BET surface area, but also improved the gasification reactivity of char.

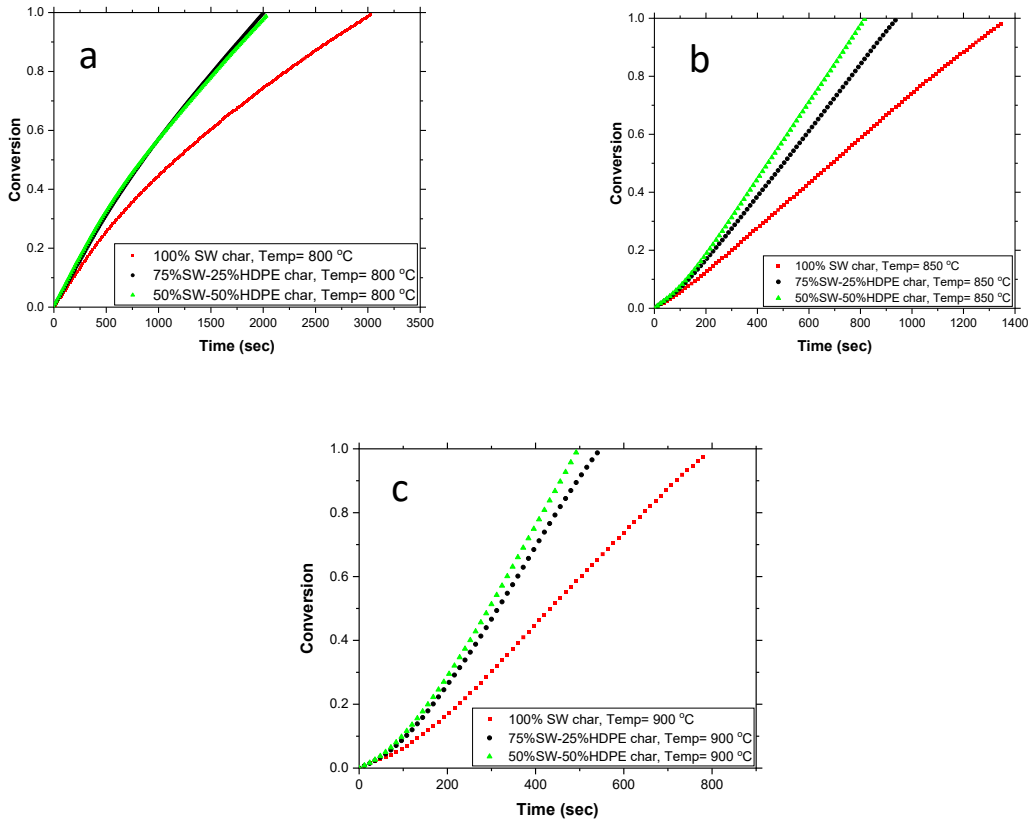

Figure 5.7: Conversion vs time graphs for CO_2 gasification of chars formed using SW and HDPE blends at different temperatures:(a)= $800\,^0C$, (b)= $850\,^0C$, (c)= $900\,^0C$

5.6.1 Evaluation of kinetic parameters

Kinetic parameters for the gasification of chars, were obtained using experimental data and then re-evaluated using the model proposed in chapter 3 taking into account the diffusional resistances within the crucible. The scheme of the methodology used is similar to the one proposed in section 3.6. First the conversion vs time data gained experimentally was used to obtain kinetic parameters using the RPM model. For all the three biochars, the value of structural parameter(ψ) was chosen to be 4. These parameters where then inputted into the MATLAB code and bisection method was used to determine the improved parameters. The only difference between the char properties mentioned in Table 4.5 and the once used for these samples was in the BET surface area and the char sample height which in this case changed to .224 mm as the sample used was only 3.5 mg. The values of kinetic parameters are listed in Table 5.4. It can be seen that increasing the blending ratio decreases the activation energy of the gasification reactions.

Table 5.4: Kinetic parameters calculated from experimental data and then re-evaluated using the TGA model

Sample name	Experimentally calculated kinetic parameters	Model-based kinetic parameters
100%SW char	$A_0 = 1.26 \cdot 10^1\, m\, s^{-1}$, $E_A = 151.237\, kJ\, mol^{-1}$	$A_0 = 1.48 \cdot 10^1\, m\, s^{-1}$, $E_A = 172.231\, kJ\, mol^{-1}$
75% SW-25% HDPE char	$A_0 = 1.07 \cdot 10^1\, m\, s^{-1}$, $E_A = 147.538\, kJ\, mol^{-1}$	$A_0 = 1.30 \cdot 10^1\, m\, s^{-1}$, $E_A = 168.214\, kJ\, mol^{-1}$
50% SW-50% HDPE char	$A_0 = 7.11\, m\, s^{-1}$, $E_A = 143.597\, kJ\, mol^{-1}$	$A_0 = 1.22 \cdot 10^1\, m\, s^{-1}$, $E_A = 165.488\, kJ\, mol^{-1}$

5.7 Conclusion

In this chapter synergies between SW and HDPE and its impact on biochar reactivity were evaluated. First, different blends of SW and HDPE were pyrolysed in a TGA and the weight loss and DTG curves of the samples were studied. All the blends, wore the characteristics of their parental curves. To evaluate the synergistic effects between them, a new term ΔW was defined. The plots of ΔW for the three different blends, suggest that the synergistic mechanism taking place between SW and HDPE was as follows: Initially the HDPE softens and coats the SW particles, which traps the volatiles released from its decomposition. This leads to a negative ΔW. The primary radicals formed from cellulose decomposition abstract hydrogen from HDPE radicals thus stabilizing the primary products and promoting the chain scission of HDPE polymer. This in turn leads to a large release of volatiles and increases the ΔW to positive and at last the radicals formed from HDPE decomposition catalyze the lignin decomposition which in turns reduces the final char yield and leads to negative ΔW finally.

The tube furnace was then used to form a larger quantity of chars for further characterization and experiments. The results from solid's yield at the end of tube furnace experiments also concur with the fact that char yield is lower when SW is co-pyrolysed along with HDPE. Upon characterization of this char it waa found that, chars produced from blends have higher carbon content and a lower oxygen content within them. Co-pyrolysis also increased the BET surface area of the chars as more volatiles were released which lead to the rupturing of fibrous fragments and opened more pores within the char particles. Finally, gasification experiments of these chars displayed that the chars formed using blends had higher reactivity based on its high carbon content and high BET surface area.

Chapter 6

Summary and Future Work

6.1 Summary

The present work was divided into two major parts. Gasification of chars using CO_2 was studied using a Thermogravimetric Analyser (TGA) in the first part of this project. TGA is used extensively for predicting reaction kinetic paramaters of gasification of chars ,as it provides the added benefits of directly measuring the char weight loss with time in a safe and simple manner. However, build up of gas within the empty space above the char sample has significant diffusional effects which are often neglected while studying kinetics. Therefore a numerical model of the TGA capturing the phenomenon within the crucible was proposed to determine effective kinetic parameters of the char-CO_2 boudouard reaction. The model was first written for the steady state reaction of non-porous char particles and solved in MATLAB software. The results were matched against 3-D CFD simulations of a particle resolved bed. After validation of the model, the model was extended to porous particles wherein evolution of particle diameter and particle porosity with time and diffusion of gases within the pores of the particles were taken into account. Isothermal TGA experiments of the biochar were perfomed at three different temperatures. The gained data was then converted to conversion vs time which was then used to obtain the kinetic parameters using the RPM model.

The activation energy of the char-CO_2 reaction from the experiments was obtained as 190.528 $kJ\,mol^{-1}$. These parameters were then inputted into the model and Bisection method was then used to re-evaluate new parameters such that the the relative error of the weighted average $Y_{CO_2,pm}$ within the crucible was less than $< 10^{-4}$ and the curves predicted by the model were in conjunction with the experimental curves. The activation energy of the Boudouard reaction using the model was re-evaluated to be 206.731 $kJ\,mol^{-1}$ which was 8.5% higher than the one obtained experimentally.

In the second part of this work mixtures of Softwood and HDPE were formed by blending different weight ratios of HDPE. The mixtures along with the pure samples were then pyrolysed using the TGA and the synergistic effects were studied using a term called as ΔW which is the difference between experimentally obtained and the theoretically determined weight loss of the mixture. The results showed that significant synergistic effects occurred between the two samples when they were co-pyrolysed together. This was reasoned based on the coating effect of the plastic on biomass particles, which leads to the biomass radicals abstracting hydrogen from the plastic radicals. As a result a lower yield of char is obtained. The tube furnace experiments confirmed this. In the last sections of this part, char produced using blends was characterized using Elemental analysis, BET surface area tests and SEM imaging and after characterization was gasified in CO_2 atmosphere to compare their reactivity and obtain kinetic parameters similar to the first part. Results showed that co-pyrolysis significantly improved the properties of the char obtained by increasing the carbon content and the BET surface area which in turn improved their gasification rates. A 3.9% decrease in the activation energy was also observed upon increasing the blending ratio of the HDPE from 0 to 50%.

6.2 Future Work

The future work based on this study, which can be performed in order to help commercialize the gasification technology in the near future is:

1. An enhanced kinetic model effectively capturing the structural change of char and also taking into consideration the catalytic effects of the mineral content of char needs to be formed.

2. Method of pyrolysis of biomass has an evident effect on the char reactivity. Therefore optimization of parameters of biomass pyrolysis is needed so as to form char with higher reactivity.

3. Based on the synergistic effects, different feedstocks can be tested so as to improve the quality of products such as bio-oil and biochar. Catalysts can also play an important role in selectivity of the products from the co-pyrolysis of biomass and plastics and therefore more study in this area is required.

Bibliography

[1] T. Bhaskar et al. "Thermochemical Conversion of Biomass to Biofuels". In: *Biofuels*. Academic Press, 2011. Chap. 3, pp. 51–77.

[2] *International Energy Outlook*. U.S. department of Energy, 2019.

[3] H.C. Ong et al. "A state-of-the-art review on thermochemical conversion of biomass for biofuel production: A TG-FTIR approach". In: *Energy Conversion and Management* 209 (2020), p. 112634.

[4] Z. Lai et al. "A study on municipal solid waste (MSW) combustion in N_2/O_2 and CO_2/O_2 atmosphere from the perspective of TGA". In: *Energy* 36 (2011), pp. 819–824.

[5] X. Zheng et al. "Hydrogen and syngas production from municipal solid waste (MSW) gasification via reusing CO_2". In: *Applied Thermal Engineering* 144 (2018), pp. 242–247.

[6] C.D. Blasi. "Combustion and gasification rates of lignocellulosic chars". In: *Progress in Energy and Combustion Science* 35 (2009), pp. 121–140.

[7] P.I Gonzalez and B.G. Rong. "A review of the current state of biofuels production from lignocellulosic biomass using thermochemical conversion routes". In: *Chinese Journal of Chemical Engineering* 27 (2019), pp. 1523–1535.

[8] S.V. Vassilev et al. "An overview of the chemical composition of biomass". In: *Fuel* 89 (2010), pp. 913–933.

[9] Antonio Tursi. “A review on biomass: importance, chemistry, classification, and conversion”. In: *Biofuel research journal* 22 (2019), pp. 962–979.

[10] F.X. Collard and J. Blin. “A review on pyrolysis of biomass constituents: Mechanisms and composition of the products obtained from the conversion of cellulose, hemicelluloses and lignin”. In: *Renewable and Sustainable Energy Reviews* 38 (2014), pp. 594–608.

[11] C. Yang and X. Liu. “Composition of plant biomass and its impact on pretreatment”. In: *Advances in 2nd generation of bioethanol production*. Woodhead publishing, 2021. Chap. 5, pp. 71–85.

[12] W.H. Chen et al. “Independent parallel pyrolysis kinetics of cellulose, hemicelluloses and lignin at various heating rates analyzed by evolutionary computation”. In: *Energy Conservation and Management* 221 (2020), p. 113165.

[13] G. Tao et al. “Biomass properties in association with plant species and assortments I: A synthesis based on literature data of energy properties”. In: *Renewable and Sustainable Energy Reviews* 16 (2012), pp. 3481–3506.

[14] J. Cai et al. “Review of physicochemical properties and analytical characterization of lignocellulosic biomass”. In: *Renewable and Sustainable Energy Reviews* 76 (2017), pp. 309–322.

[15] N.L. Panwar, R. Kothari, and V.V. Tyagi. “Thermo chemical conversion of biomass-Eco friendly energy routes”. In: *Renewable and Sustainable Energy Reviews* 16 (2012), pp. 1801–1816.

[16] B. Sajjadi, A.A.A. Raman, and H. Arandiyan. “A comprehensive review on properties of edible and non-edible vegetable oil-based biodiesel: Composition, specifications and prediction models”. In: *Renewable and Sustainable Energy Reviews* 63 (2016), pp. 62–92.

[17] T. Damartzis and A. Zabaniotou. "Thermochemical conversion of biomass to second generation biofuels through integrated process design—A review". In: *Renewable and Sustainable Energy Reviews* 15 (2011), pp. 366–378.

[18] R.E.H. Sims et al. "An overview of second generation biofuel technologies". In: *Bioresource technology* 101 (2010), pp. 1570–1580.

[19] P. Binod et al. "Enzymes for second generation biofuels: Recent developments and future perspectives". In: *Bioresource Technology Reports* 5 (2019), pp. 317–325.

[20] T. Nussbaumer. "Combustion and Co-combustion of Biomass:Fundamentals, Technologies, and Primary Measures for Emission Reduction". In: *Energy and Fuels* 17 (2003), pp. 1510–1521.

[21] A. Demirbas. "Pyrolysis Mechanisms of Biomass Materials". In: *Energy Sources* 31 (2009), pp. 1186–1193.

[22] A.R.K. Gollakota, N. Kishore, and S. Gu. "A review on hydrothermal liquefaction of biomass". In: *Renewable and Sustainable Energy Reviews* 81 (2018), pp. 1378–1392.

[23] A. Mathanker et al. "Hydrothermal liquefaction of lignocellulosic biomass feedstock to produce biofuels: Parametric study and products characterization". In: *Fuel* 271 (2020), p. 117534.

[24] P. Basu. *Biomass Gasification, Pyrolysis and Torrefaction.* second. Academic Press, 2013.

[25] A.T. Ubando et al. "A comprehensive review of life cycle assessment (LCA) of microalgal and lignocellulosic bioenergy products from thermochemical processes". In: *Bioresource Technology* 291 (2019), p. 121837.

[26] A.U.Zaman. "Comparative study of municipal solid waste treatment technologies using life cycle assessment method". In: *Int. J. Environ. Sci. Tech.* 7(2) (2010), pp. 225–234.

[27] S.Ciuta, D.Tsiamis, and M.J. Castaldi. *GASIFICATION OF WASTE MATERIALS*. Academic Press, 2018.

[28] Massimiliano Materazzi and Pier Ugo Foscolo. "Waste gasification processes for SNG production". In: *Substitute Natural Gas from Waste*. Ed. by Hermann Hofbauer and Massimiliano Materazzi. Academic Press, 2019. Chap. 7, pp. 105–160.

[29] M.W. Islam. "Effect of different gasifying agents (steam, H_2O_2, oxygen, CO_2 and air) on gasification parameters". In: *International journal of hydrogen energy* 45 (2020), pp. 31760–31774.

[30] A.M. Parvez et al. "Utilization of CO_2 in thermochemical conversion of biomass for enhanced product properties: A review". In: *Journal of CO_2 Utilization* 40 (2020), p. 101217.

[31] U. Arena. "Process and technological aspects of municipal solid waste gasification. A review". In: *Waste Management* 32 (2012), pp. 625–639.

[32] A. Chaurasia. "Modeling, simulation and optimization of downdraft gasifier: Studies on chemical kinetics and operating conditions on the performance of the biomass gasification process". In: *Energy* 116 (2016), pp. 1065–1069.

[33] S.S. Siwal et al. "Energy production from steam gasification processes and parameters that contemplate in biomass gasifier – A review". In: *Bioresource Technology* 297 (2020), p. 122481.

[34] H.S. Fogler. *Elements of Chemical Reaction Engineering*. fourth. Pearson Education, Inc, 2006.

[35] J. Szekely, J.W. Evans, and H.Y. Sohn. *GAS-SOLID REACTIONS*. Academic Press, 1976. ISBN: 0-12-680850-3.

[36] N. Mahinpey and A. Gomez. "Review of gasification fundamentals and new findings: Reactors, feedstock, and kinetic studies". In: *Chemical Engineering Science* 148 (2016), pp. 14–31.

[37] C. Guizani, F.J.E. Sanz, and S. Salvador. "Influence of temperature and particle size on the single and mixed atmosphere gasification of biomass char with H_2O and CO_2". In: *Fuel Processing Technology* 134 (2015), pp. 175–188.

[38] R. Roncancio and J.P. Gore. "CO_2 char gasification: A systematic review from 2014 to 2020". In: *Energy Conversion and Management: X* 10 (2020), p. 10060.

[39] M. Morin, S. Pecate, and M. Hemati. "Experimental study and modelling of the kinetic of biomass char gasification in a fluidized bed reactor". In: *Chemical Engineering Research and Design* 131 (2018), pp. 488–505.

[40] Z. Huang et al. "Kinetic studies of char gasification by steam and CO_2 in the presence of H_2 and CO". In: *Fuel Processing Technology* 91 (2010), pp. 843–847.

[41] G. Wang et al. "Experimental and modeling studies on CO2 gasification of biomass chars". In: *Energy* 114 (2016), pp. 143–154.

[42] J.P. Hernandez et al. "An experimental study of CO2 gasification kinetics during activation of a spent tyre pyrolysis char". In: *Chemical Engineering Research and Design* 149 (2019), pp. 129–137.

[43] J. Szekely and J.W. Evans. "A structural model for gas-solid reactions with a moving boundary". In: *Chemical Engineering Science* 25 (1970), pp. 1091–1107.

[44] S. Schulze et al. "Novel intrinsic-based submodel for char particle gasification in entrained-flow gasifiers: Model development, validation and illustration". In: *Applied Energy* 164 (2016), pp. 805–814. ISSN: 0306-2619.

[45] I.I. Ahmed and A.K. Gupta. "Kinetics of woodchips char gasification with steam and carbon dioxide". In: *Applied Energy* 88 (2011), pp. 1613–1619.

[46] S.K. Bhatia and D.D. Perlmutter. "A random pore model for fluid-solid reactions: I. Isothermal, kinetic control". In: *AIChE* 26 (1980), pp. 379–386.

[47] L. Lin and M. Strand. "Investigation of the intrinsic CO_2 gasification kinetics of biomass char at medium to high temperatures". In: *Applied Energy* 109 (2013), pp. 220–228.

[48] M. Liu et al. “Char reactivity and kinetics based on the dynamic char structure during gasification by CO_2”. In: *Fuel Processing Technology* 211 (2021), p. 106583.

[49] M. Malekshahian and J.M. Hill. “Kinetic Analysis of CO_2 Gasification of Petroleum Coke at High Pressures”. In: *Energy and Fuels* 25 (2011), pp. 4043–4048.

[50] I. Sircar et al. “Experimental and modeling study of pinewood char gasification with CO_2”. In: *Fuel* 119 (2014), pp. 38–46.

[51] Y. Guo et al. “Kinetics of steam gasification of in-situ chars in a micro fluidized bed”. In: *International Journal of Hydrogen Energy* 41 (2016), pp. 15187–15198.

[52] M. Cortazar et al. “Experimental study and modeling of biomass char gasification kinetics in a novel thermogravimetric flow reactor”. In: *Chemical Engineering Journal* 396 (2020), p. 125200.

[53] J.L. Zhang et al. “A Modified Random Pore Model for the Kinetics of Char Gasification”. In: *Bioresources* 9(2) (2014), pp. 3497–3507.

[54] Y. Zhang et al. “Proposal of a semi-empirical kinetic model to reconcile with gasification reactivity profiles of biomass chars”. In: *Fuel* 87 (2008), pp. 475–481.

[55] R.B. Woodruff and A.W. Weimer. “A novel technique for measuring the kinetics of high-temperature gasification of biomass char with steam”. In: *Fuel* 103 (2013), pp. 749–757.

[56] L. Zhou et al. “Kinetic study on CO2 gasification of brown coal and biomass chars: reaction order”. In: *Fuel* 173 (2016), pp. 311–319.

[57] S. Nilsson, A.G. Barea, and D.F. Cano. “Gasification reactivity of char from dried sewage sludge in a fluidized bed”. In: *Fuel* 92 (2012), pp. 346–353.

[58] S. Nilsson et al. “Gasification kinetics of char from olive tree pruning in fluidized bed”. In: *Fuel* 125 (2014), pp. 192–199.

[59] F. Wang et al. “Characterization of coal char gasification with steam in a micro-fluidized bed reaction analyzer”. In: *Fuel Processing Technology* 141 (2016), pp. 2–8.

[60] S. Tong et al. "A kinetic study on lignite char gasification with CO_2 and H_2O in a fluidized bed reactor". In: *Applied Thermal Engineering* 147 (2019), pp. 602–609.

[61] F. Keller, F. Kuster, and B. Meyer. "Determination of coal gasification kinetics from integral drop tube furnace experiments with steam and CO_2". In: *Fuel* 218 (2018), pp. 425–438.

[62] D.H. Ahn et al. "Gasification kinetics of an Indonesian sub-bituminous coal-char with CO_2 at elevated pressure". In: *Fuel* 80 (2001), pp. 1651–1658.

[63] S. Kajitani, S. Hara, and H. Matsuda. "Gasification rate analysis of coal char with a pressurized drop tube furnace". In: *Fuel* 81 (2002), pp. 539–546.

[64] K. Matsumoto et al. "Gasification reaction kinetics on biomass char obtained as a by-product of gasification in an entrained-flow gasifier with steam and oxygen at 900–1000 ^0C". In: *Fuel* 88 (2009), pp. 519–527.

[65] M. Zhai et al. "Characteristics of rice husk char gasification with steam". In: *Fuel* 158 (2015), pp. 42–49.

[66] V. Gonzalez et al. "Experimental investigations on lignite char gasification kinetics using a pressurized drop tube reactor". In: *Fuel* 224 (2018), pp. 348–356.

[67] O. Senneca. "Kinetics of pyrolysis, combustion and gasification of three biomass fuels". In: *Fuel Processing Technology* 88 (2007), pp. 87–97.

[68] D.L. Gonzalez et al. "Gasification of lignocellulosic biomass char obtained from pyrolysis: Kinetic and evolved gas analyses". In: *Energy* 71 (2014), pp. 456–467.

[69] A. Gupta, S.K. Thengane, and S. Mahajani. "CO_2 gasification of char from lignocellulosic garden waste: Experimental and kinetic study". In: *Bioresource Technology* 263 (2018), pp. 180–191.

[70] R.S. Xu et al. "Gasification behaviors and kinetic study on biomass chars in CO_2 condition". In: *Chemical Engineering Research and Design* 107 (2016), pp. 34–42.

[71] J. Tanner and S. Bhattacharya. "Kinetics of CO_2 and steam gasification of Victorian brown coal chars". In: *Chemical Engineering Journal* 285 (2016), pp. 331–340.

[72] A.G. Barea, P. Ollero, and C.F. Baco. "Diffusional Effects in CO_2 Gasification Experiments with Single Biomass Char Particles. 1. Experimental Investigation". In: *Energy and Fuels* 20 (2006), pp. 2202–2210.

[73] P. Ollero et al. "Diffusional effects in TGA gasification experiments for kinetic determination". In: *Fuel* 81 (2002), pp. 1989–2000.

[74] O. Levenspiel. *Chemical reaction engineering*. Wiley, 1999.

[75] S. Schulze et al. "Heat and mass transfer within thermogravimetric analyser: From simulation to improved estimation of kinetic data for char gasification". In: *Fuel* 187 (2017), pp. 338–348. ISSN: 0016-2361.

[76] B.B. Uzoejinwa et al. "Co-pyrolysis of biomass and waste plastics as a thermochemical conversion technology for high-grade biofuel production: Recent progress and future directions elsewhere worldwide". In: *Energy Conversion and Management* 163 (2018), pp. 468–492.

[77] S. Xiong et al. "Study on the co-pyrolysis of high density polyethylene and potato blends using thermogravimetric analyzer and tubular furnace". In: *Journal of Analytical and Applied Pyrolysis* 112 (2015), pp. 66–73.

[78] G. Lopez et al. "Recent advances in the gasification of waste plastics. A critical overview". In: *Renewable and Sustainable Energy Reviews* 82 (2018), pp. 576–596.

[79] S.D. Gunasee et al. "Pyrolysis and combustion of municipal solid wastes: Evaluation of synergistic effects using TGA-MS". In: *Journal of Analytical and Applied Pyrolysis* 121 (2016), pp. 50–61.

[80] P. Lu et al. "Synergistic effects on char and oil produced by the co-pyrolysis of pinewood, polyethylene and polyvinyl chloride". In: *Fuel* 230 (2018), pp. 359–367.

[81] L. Chen et al. "Synergistic effect on thermal behaviour and char morphology analysis during co-pyrolysis of paulownia wood blended with different plastics waste". In: *Applied Thermal Engineering* 111 (2017), pp. 834–846.

[82] Y. Zheng et al. "Study of the thermal behavior, kinetics, and product characterization of biomass and low-density polyethylene co-pyrolysis by thermogravimetric analysis and pyrolysis-GC/MS". In: *Journal of Analytical and Applied Pyrolysis* 133 (2018), pp. 185–197.

[83] K.G. Burra and A.K. Gupta. "Kinetics of synergistic effects in co-pyrolysis of biomass with plastic wastes". In: *Applied Energy* 220 (2018), pp. 408–418.

[84] J.N.V. Salvilla et al. "Synergistic co-pyrolysis of polyolefin plastics with wood and agricultural wastes for biofuel production". In: *Applied Energy* 279 (2020), p. 115668.

[85] R. Chen et al. "Thermal behaviour and kinetic study of co-pyrolysis of microalgae with different plastics". In: *Waste Management* 126 (2021), pp. 331–339.

[86] X. Wang et al. "Synergistic effects of biomass and polyurethane co-pyrolysis on the yield, reactivity, and heating value of biochar at high temperatures". In: *Fuel Processing Technology* 194 (2019), p. 106127.

[87] I.I. Ahmed, N. Nipattummakul, and A.K. Gupta. "Characteristics of syngas from co-gasification of polyethylene and woodchips". In: *Applied Energy* 88 (2011), pp. 165–174.

[88] K.G. Burra and A.K. Gupta. "Synergistic effects in steam gasification of combined biomass plastic waste mixtures". In: *Applied Energy* 211 (2018), pp. 230–236.

[89] M.K. Gill. "Thermo-Catalytic Reforming of Woody Biomass". MA thesis. University of Alberta, 2020.

[90] S.R. Turns. *An Introduction to Combustion:concepts and applications*. second. McGraw-Hill, 2000. ISBN: 0-07-230096-5.

[91] D.A. Nield and A. Bejan. *Convection in Porous Media*. Springer. ISBN: 978-3-319-49562-0.

[92] Hugo S. Caram and Neal R. Amundson. "Diffusion and Reaction in a Stagnant Boundary Layer about a Carbon Particle". In: *Industrial Engineering Chemistry Fundamentals* 16.2 (1977), pp. 171–181. DOI: 10.1021/i160062a001.

[93] P.A. Nikrityuk and B. Meyer. *Gasification Processes:Modeling and Simulation*. John Wiley Sons, 2014. ISBN: 9783527673209.

[94] K. Weber and P. Quicker. "Properties of biochar". In: *Fuel* 217 (2018), pp. 240–261.

[95] R. Wu et al. "Biomass char particle surface area and porosity dynamics during gasification". In: *Fuel* 264 (2020), p. 116883.